Manuscript Click here to view linked References

Oligomerization and positive feedback on membrane recruitment encode dynamically stable PAR-3 asymmetries in the *C. elegans* zygote.

Charlie Lang[1,2,4], Ondrej Maxian[1], Alexander Anneken[1] and Edwin Munro[1,2,]

1 *Department of Molecular Genetics and Cell Biology, University of Chicago, Chicago, IL 60637*
2 *Committee on Genetics, Genomics and Systems Biology, University of Chicago, Chicago, IL 60637*
3 *Institute for Biophysical Dynamics, University of Chicago, Chicago, IL 60637*
4 *Current address: Department of Molecular and Cellular Physiology, Stanford University, Stanford, CA 94305*
5 *Correspondence to emunro@uchicago.edu*

Contact info:
Edwin Munro
Molecular Genetics and Cell Biology
University of Chicago
920 E 58th St
CLSC 901
Phone: (773)-702-6221
Fax: (773) 702-3172
email: emunro@uchicago.edu

Abstract

Studies of PAR polarity have emphasized a paradigm in which mutually antagonistic PAR proteins form complementary polar domains in response to transient cues. A growing body of work suggests that the oligomeric scaffold PAR-3 can form unipolar asymmetries without mutual antagonism, but how it does so is largely unknown. Here we combine single molecule analysis and modeling to show how the interplay of two positive feedback loops promote dynamically stable unipolar PAR-3 asymmetries in early *C. elegans* embryos. First, the intrinsic dynamics of PAR-3 membrane binding and oligomerization encode negative feedback on PAR-3 dissociation. Second, membrane-bound PAR-3 promotes its own recruitment through a mechanism that requires the anterior polarity proteins CDC-42, PAR-6 and PKC-3. Using a kinetic model tightly constrained by our experimental measurements, we show that these two feedback loops are individually required and jointly sufficient to encode dynamically stable and locally inducible unipolar PAR-3 asymmetries in the absence of posterior inhibition. Given the central role of PAR-3, and the conservation of PAR-3 membrane-binding, oligomerization, and core interactions with PAR-6/aPKC, these results have widespread implications for PAR-mediated polarity in metazoa.

Introduction

The PAR proteins are a highly conserved network of proteins that govern cell polarity in many different cells and tissues across the metazoa[1,2]. In all of these contexts, the PAR proteins become asymmetrically enriched in response to transient local cues. These asymmetries are reinforced through feedback loops in which PAR proteins locally promote or inhibit one another's accumulation. Asymmetrically enriched PARs then act through different downstream targets to elaborate functionally polarized states. While the local polarizing cues vary widely across different contexts, the interactions among PAR proteins that govern the response to these cues is more highly conserved. Thus, a central challenge is to understand how systems of feedback among the PARs encode their ability to form and stabilize spatial patterns of enrichment that define functional polarity.

The one-cell *C. elegans* embryo (i.e. the zygote) has been a powerful model system for uncovering the core molecular circuitry that governs PAR polarity. During polarization of the zygote, two sets of PAR proteins become asymmetrically enriched in complementary anterior and posterior membrane domains. The anterior aPARs include the oligomeric scaffold PAR-3, the adaptor PAR-6, the kinase PKC-3, and the small GTPase CDC-42. The posterior pPARs include the kinase PAR-1, a *C. elegans*-specific protein called PAR-2, and a putative CDC-42 GAP called CHIN-1.

Polarization proceeds through two distinct phases, called establishment and maintenance[3], which correspond respectively to mitotic interphase and mitosis. Before polarization, aPARs are uniformly enriched at the cell surface, while pPARs are largely cytoplasmic. During polarity

establishment, a local sperm-derived cue triggers the redistribution of aPARs and pPARs into complementary domains. The sperm cue is closely associated with a centrosomal microtubule organizing center called the sperm MTOC that forms near the site of sperm entry [4,5]. The sperm MTOC acts through the aurora kinase AIR-1 [6–9] to trigger actomyosin-based cortical flows that transport aPARs towards the anterior pole [10,11]. In addition, astral microtubules associated with the sperm MTOC promote the local accumulation of pPARs PAR-1 and PAR-2 on the posterior membrane [12,13].

During mitosis, the centrosomes (thus the polarity cue) migrate to the cell center. However, PAR asymmetries are maintained through mitosis despite continuous diffusion and exchange of PAR proteins between the cytoplasm and the cell membrane [14,15]. The prevailing model is that PAR asymmetries are maintained by a network of mutually antagonistic interactions in which aPARs and pPARs act locally to inhibit one another's accumulation (reviewed in Lang and Munro [2], Figure 1A). Both PAR-3 and active CDC-42 are required for local recruitment of PAR-6/PKC-3 into an active complex with CDC-42 [16,17]. Active PKC-3 inhibits local accumulation of pPARs, including PAR-1 and CHIN-1 [12,17–22]. PAR-1 inhibits local accumulation of PAR-3 [12,23], while CHIN-1 inhibits local activation of CDC-42 [17,22,24]. Because both PAR-3 and CDC-42 are required for local recruitment of PAR-6/PKC-3 during mitosis, either PAR-1 or CHIN-1 is sufficient to prevent posterior recruitment of PAR-6/PKC-3.

Strikingly, in zygotes that lack both PAR-1 and CHIN-1, all other pPARS are restricted to the cytoplasm, the aPARs CDC-42, PAR-6 and PKC-3 are uniformly enriched, but PAR-3 asymmetries still form and persist through mitosis [17] (Figure 1B). PAR-3 is the keystone member

of the PAR network without which all other PAR asymmetries are lost. Segregation of PAR-3 is a first step in polarization in many different contexts [12,25–28] . Thus, additional mechanisms must exist to maintain monopolar PAR-3 asymmetries in the absence of mutual antagonism with pPARs and these mechanisms must also contribute to shaping PAR asymmetries in normal embryos. Importantly, monopolar PAR-3 asymmetries have also been observed under wild-type conditions in other contexts, including in neuroblast stem cells [29–31] and in mammalian hippocampal neurons [32] and *Drosophila* male germline cells [33]. However, their molecular bases remain unknown.

A key feature of PAR-3 is its ability to form oligomers at the cell membrane. PAR-3 self-associates through a conserved N-terminal PB1-like domain, called the CR1 domain [34]. The purified CR1 domain assembles head to tail into helical filaments in vitro [35,36]. While PAR-3 contains multiple domains that can support direct binding to plasma membranes [37,38], deletion or mutation of the CR1 domain prevents strong accumulation of PAR-3 in *C. elegans* [37] and other systems [34,35,38], and induces defects in embryonic polarity [16,37,39]. Oligomerization of PAR-3 plays an essential role in polarity establishment by coupling PAR-3 to the actomyosin cortex, facilitating segregation of PAR-3 and other aPARs by anterior-directed cortical actomyosin flows [16,26,39–41]. But it remains unknown whether oligomerization of PAR-3 plays additional roles in polarity maintenance, and in particular, whether and how oligomerization of PAR-3 might contribute to stabilizing PAR-3 asymmetries in the absence of mutual antagonism among the PARs.

Here, we combine single molecule imaging and particle tracking analysis with genetic manipulations and modeling to reveal a mechanism for self-stabilizing PAR-3 asymmetries in the *C. elegans* zygote. We show that PAR-3 asymmetries are maintained despite the continuous rapid exchange of subunits with PAR-3 oligomers. We find that two key factors maintain PAR-3 asymmetries in the absence of posterior inhibition: First, size-dependent membrane binding avidity of PAR-3 oligomers confers negative dependence of PAR-3 dissociation rate on local PAR-3 density – a form of positive feedback. Second, enhanced recruitment of PAR-3 to membranes where PAR-3 is already enriched, which requires the aPARs CDC-42, PAR-6 and PKC-3, provides a second form of positive feedback. Mathematical models, tightly constrained by our experimental measurements, show that the combination of negative feedback on dissociation and positive feedback on recruitment ensure the coexistence of two dynamically stable states: an unpolarized state, characterized by uniformly high levels of PAR-3, and a polarized state, characterized by asymmetric enrichment of PAR-3. The model predicts that transient local depletion of PAR-3, as occurs in response to the sperm cue during polarity establishment, can induce a transition between unpolarized and polarized states. Thus, self-stabilizing PAR-3 asymmetries encode a lasting memory of PAR distributions induced by a transient polarizing cue. Together, these results reveal a novel mechanism for stabilizing PAR-3 asymmetries in the absence of mutual antagonism, which depends on core dynamics of PAR-3 oligomer assembly and interactions with its conserved partners CDC-42, PAR-6 and PKC-3. We propose that similar mechanisms may underlie the stabilization of unipolar PAR asymmetries in other contexts.

Results

PAR-3 asymmetries approach a dynamic steady state during maintenance phase.

As a first step to identifying mechanisms that maintain PAR-3 asymmetries in the absence of posterior inhibition by PAR-1, we used near-TIRF microscopy and single particle analysis to quantify dynamic changes in PAR-3 oligomer size and density during polarization in homozygous *par-1* mutant embryos (Figure 2A-D, Movie S1, see Methods). Consistent with previous reports, during polarity establishment, mean oligomer size, oligomer density, and overall density of PAR-3 increased steadily on the anterior cortex and decreased on the posterior cortex as cortical flows transport PAR-3 towards the anterior pole [39,41]. At the onset of maintenance phase, mean oligomer size and overall density of PAR-3 began to decrease, while oligomer density remained roughly constant. The rate of decrease was initially fast, but slowed progressively during maintenance phase, such that oligomer size and overall density approached plateaus at ~50% of their maximum values in late establishment phase. We observed similar PAR-3 oligomer dynamics in control (*par-1* heterozygote) embryos and throughout the cortex in embryos depleted of SPD-5 by RNAi, which lack a functional sperm cue and fail to establish polarity (Figure S1, Movie S1).

The slow approach to plateau levels of PAR-3 density and mean oligomer size could reflect either (a) the gradual disassembly of otherwise stable PAR-3 oligomers, or (b) the approach to a steady state governed by a dynamic balance of more rapid membrane-binding and oligomer-assembly kinetics. Consistent with the latter possibility, after photobleaching the entire cortex, total fluorescence in detected PAR-3 oligomers recovered to ~ 60% of the pre-bleach value with a mean half-time of 8.52 +\- 4.3 seconds (Figure 2F; n = 4 embryos; Movie S2). Direct

inspection of the recovery time series suggests that individual PAR-3 oligomers recover fluorescence on similarly fast timescales (orange arrowheads in Fig 2E). These data suggest that PAR-3 asymmetries approach a steady state that is maintained in the face of more rapid exchange of cytoplasmic PAR-3 with the membrane and with membrane-bound oligomers.

Intrinsic kinetics of membrane binding and oligomerization produce an approximately exponential distribution of PAR-3 oligomer sizes.

To probe the mechanisms underlying this dynamic steady state, we used single molecule imaging and particle tracking analysis to characterize the kinetics of PAR-3 membrane binding and oligomerization in relation to slowly changing distributions of PAR-3 oligomers. As a framework for this analysis, we considered a simple kinetic model (Figure 3A, Modeling Supplement) in which: (a) cytoplasmic PAR-3 monomers bind reversibly to the plasma membrane, (b) membrane-bound PAR-3 monomers form small oligomers, and (c) oligomers dissociate from the membrane with size-dependent kinetics – i.e. with an off rate that decreases with oligomer size. For reasons justified later (see Modeling Supplement and below), we assume that direct binding of cytoplasmic monomers to PAR-3 oligomers, and binding of cytoplasmic PAR-3 oligomers to the membrane can both be neglected.

We focused initially on measuring the intrinsic kinetics of PAR-3 membrane binding and oligomerization to confirm the model's core assumptions, constrain kinetic parameters, and compare key model predictions to experimental observations. If oligomers dissociate much more slowly than monomers, as we confirm below (see Figure 4C), then the steady state distribution of oligomer sizes should be approximately exponential, given by $A_n \sim A_1 \alpha^{n-1}$, where A_n is the

density of oligomers with n subunits, $\alpha = \frac{k_{pol}}{k_{dep}} A_1$ measures oligomerization strength, and the mean oligomer size is $s = \frac{1}{1-\alpha}$. Moreover, both oligomerization strength and mean oligomer size should increase with density of membrane-bound PAR-3 (see Modeling Supplement for details).

To test these predictions, we measured the distributions of PAR-3 oligomer sizes on anterior and posterior membranes in *par-1* mutant embryos expressing endogenously-tagged PAR-3::GFP at quasi-steady state during late maintenance phase. We used the intensities of single PAR-3::GFP molecules, measured in the same embryos after photobleaching, as an internal size standard (Figure 3C-E, see Methods). Consistent with prediction, both the anterior and posterior distributions of oligomer sizes were well-fit by single-exponential functions (Figure 3F). The estimated oligomerization strengths ($\alpha_A = 0.730 \pm 0.052$, $\alpha_P = 0.424 \pm 0.054$) and mean oligomer sizes ($s_A = 3.48 \pm 0.65$, $s_P = 1.65 \pm 0.16$) were higher on the anterior cortex where total PAR-3 density is higher (Figure 3G). Moreover, given the measured A:P ratio of PAR-3 densities, the ratio of oligomerization strengths (or mean oligomer sizes) agreed closely with model predictions. We also confirmed this relationship through a systematic variation of PAR-3 densities (see Figure 7D and text below). Thus, the distributions of PAR-3 oligomer sizes are consistent with a quasi-steady state governed by reversible membrane binding and polymerization.

Density-dependent oligomer size and size-dependent oligomer dissociation confers positive feedback on PAR-3 accumulation.

If mean oligomer size increases with PAR-3 density and oligomer dissociation rate decreases with size, then our model predicts that the effective dissociation rate constant for PAR-3 oligomers, defined as:

$$k_{effective} = \frac{\sum_{n=1}^{\infty} k_{off}(n) n \alpha^{n-1}}{\sum_{n=1}^{\infty} n \alpha^{n-1}}$$

should decrease with increasing oligomer size. This represents a form of positive feedback of PAR-3 on its own accumulation, whose strength depends on self-affinity of PAR-3 ($\frac{k_{pol}}{k_{dep}}$) and the size-dependence of oligomer dissociation $k_{off}(n)$. To measure the size-dependent rate of oligomer dissociation $k_{off}(n)$ during maintenance phase, we used streaming acquisition and particle tracking analysis of PAR-3 endogenously tagged with mNeonGreen (mNG::PAR-3), using the mean intensities of single molecules to calibrate estimates of oligomer size, as described above (see Methods). To improve the accuracy of particle tracking, we performed these experiments in embryos depleted of the myosin II heavy chain NMY-2 by RNAi, which increases the distance between particles by preventing the segregation of PAR-3 to the anterior pole during polarity establishment and eliminates the movements of particles driven by local actomyosin contractility (Figure 4A,B; Movie S3) To avoid the confounding effects of photobleaching, we used the intensities of oligomers in the first frame of the imaging sequence to estimate oligomer size n, and the fraction of oligomers in each size class with bound lifetimes > 1 sec to estimate $k_{off}(n)$ (see Methods). Our measurements suggest that $k_{off}(n)$ decreases sharply with oligomer size, becoming negligible for oligomer sizes > 3 subunits (Figure 4C). Using the same data to compare the intensities of PAR-3 oligomers arriving at the membrane with single molecule intensities, we also confirmed that PAR-3 recruitment is dominated by monomer binding (Figure 4D).

To quantify the strength of positive feedback due to size-dependent oligomer dissociation, we constrained the model using our estimates of both density-dependent oligomerization strengths (Figure 3G) and size-dependent dissociation $k_{off}(n)$ (Figure 4C), and then computed the dependence of the effective dissociation rate constant $k_{effective}$ on PAR-3 density at steady state (Figure 4E). Given the measured A:P ratio of PAR-3 densities, the model predicts a 3.8-fold A:P ratio in $k_{effective}$. Thus, positive feedback on PAR-3 accumulation, due to size-dependent oligomer dissociation kinetics, accounts for roughly half of the 8-fold asymmetry in PAR-3 observed in late maintenance phase.

Rapid membrane binding and slower oligomerization underlies the maintenance of PAR-3 asymmetries.

To further constrain our model's predictions, we used single molecule approaches to measure the kinetics of membrane unbinding and depolymerization. Based on the above results (Figure 2E,F; Figure 3G; Figure 4C), and previous work [17,26,39], we expect that most anterior PAR-3 molecules are associated with stably-bound slow-moving PAR-3 oligomers, and therefore their disappearance should reflect the slow kinetics of depolymerization. On the other hand, we expect that most posterior PAR-3 molecules are freely diffusing monomers, whose disappearance reflects the faster kinetics of membrane unbinding.

To confirm these expectations, we imaged single molecules of endogenously-tagged PAR-3::GFP using high laser power and streaming acquisition to ensure accurate particle tracking (Figure 5A;Movie S4; see Methods). We quantified mobilities by measuring the distribution of

root mean square displacements after 200 msec (RMSD@200; Figure 5B), and disappearance rates by constructing release curves plotting the numbers of molecules with lifetimes > t as a function of t (Figure 5C).

Consistent with our expectations, we found that posterior PAR-3 molecules have RMSD@200 distributions that are indistinguishable from those produced by simulated Brownian diffusion at ~0.1 μm^2/sec (Figure 5B right), while anterior PAR-3 molecules have RMSD_200 distributions that are well-fit by the superposition of RMSD@200 distributions measured for PAR-3 oligomers and for Brownian diffusion (Figure 5B left). Similarly, comparison of release curves revealed that anterior molecules disappear more slowly than posterior molecules, confirming that membrane unbinding is much faster than depolymerization, although photobleaching obscures the magnitude of this difference (Figure 5C). Therefore, we used the release kinetics of anterior PAR-3 molecules to estimate the rate constant for depolymerization (k_{dep}), and release kinetics of posterior PAR-3 molecules to estimate the rate constant for monomer unbinding (k_{off}).

To measure k_{dep}, we used RNAi against GFP to reduce expression of transgenic PAR-3::GFP to single molecule levels. We held the unit exposure constant (fixed laser power and 50 msec exposure time), varied the duty ratio of exposure (dr), and fit the resulting release curves with single exponentials (Figure 5E) to estimate a rate constant for disappearance k_{diss}, which reflects both depolymerization (k_{dep}) and photobleaching (k_{pb}). Plotting k_{diss} vs dr, and fitting the data to $k_{diss} = k_{dep} + k_{pb} * dr$ (Figure 5E), we obtained estimates of the rate constants for photobleaching (k_{pb}= 1.04 +/- 0.04/s) and depolymerization ($k_dep = 0.08 +/-0.02/$) (see

Methods), which agrees well with the halftime for recovery of fluorescence after photobleaching (Figure 2G).

To measure the monomer unbinding rate k_{off}, we fit release curves for single molecule data collected in streaming mode to estimate rate constants for anterior and posterior disappearance k_{diss}^{ant} and k_{diss}^{post} (Figure 5C, orange and green curves). We used k_{diss}^{ant} and our measurement of k_{dep} above to estimate $k_{pb} = k_{diss}^{ant} - k_{dep}$. Then, we used $\mathrm{k}_{\mathrm{diss}}^{\mathrm{post}}$ and k_{pb} to measure the monomer unbinding rate $\mathrm{k}_{\mathrm{off}} = \mathrm{k}_{\mathrm{diss}}^{\mathrm{post}} - \mathrm{k}_{\mathrm{pb}}$ = 2.58 +/- 0.3/sec (Figure 5F). Importantly, this estimate agrees well with the value measured above ($\mathrm{k}_{\mathrm{off}}(1)$ = 2.7/sec; Figure 4C). We measured a similar value for $\mathrm{k}_{\mathrm{off}}$ using a transgenically-expressed version of PAR-3 that lacks the N terminal CR1 oligomerization domain (PAR-3(ΔCR1)::GFP; Figure 5F, Figure S2C-D, Movie S4).

These measurements show that depolymerization is ~ 30-fold slower than membrane unbinding of PAR-3 monomers, but fast enough to explain the continuous exchange of fluorescent PAR-3 within oligomers during maintenance phase. Because the flux of monomers into and out of oligomers must balance at steady state, these measurements sharply constrain the possible contribution of direct binding of cytoplasmic PAR-3 monomers to membrane-bound oligomers. The maximum fraction of monomer recruitment due to direct binding is ~17%, although the actual value is likely to be significantly lower (see Modeling Supplement), justifying our choice to neglect direct binding in our simple model.

Finally, we used our measurements of mean oligomer size , $k_{off}(n)$, and k_{dep} to predict the overall kinetics of approach to steady state, assuming that binding kinetics are constant throughout maintenance phase. We observed good agreement between simulated and measured dynamics (Figure 5G), confirming that the intrinsic kinetics of PAR-3 membrane binding and oligomerization set the timescale of approach to steady state during maintenance.

Asymmetric monomer recruitment contributes to stabilizing PAR-3 asymmetries during maintenance phase.

We showed above that positive feedback due to size-dependent oligomer dissociation accounts for only half of the ~8-fold asymmetry in PAR-3 density observed at steady state in *par-1* mutant embryos. Moreover, theoretical analysis shows that, regardless of strength, this form of feedback is insufficient to stabilize an asymmetric distribution of membrane-bound oligomers (see Lang and Munro, 2022 [42]).Thus we wondered whether positive feedback on PAR-3 recruitment could account for the missing ~2-fold AP difference in PAR-3 densities, and if so, whether the combined effects of both forms of feedback would be sufficient to ensure the dynamic stability of PAR-3 asymmetries in the absence of posterior inhibition by PAR-1.

To test these possibilities, we first used fast single molecule imaging to measure rates of single molecule recruitment on anterior and posterior membranes during maintenance phase in wild-type and *par-1(RNAi)* embryos (Figure 6A,B; Movie S5). To avoid the confounding effects of direct binding of cytoplasmic PAR-3 to membrane-bound oligomers, we performed these measurements on a variant of PAR-3 (PAR-3(ΔCR1)::GFP lacking the conserved N-terminal CR1 domain that mediates homo-oligomerization [34,35,37]. In these experiments, single molecule

speckles that appear *de novo* on the membrane are rapidly photobleached, allowing us to detect and count many appearance events per unit area and time. To avoid counting cytoplasmic molecules that diffuse into the focal plane, we focused on molecules with tracked lifetimes >= 200 msec, for which distributions of RMSD@200ms matched those expected for membrane-bound PAR-3 molecules undergoing Brownian diffusion (Figure 6C,D; green histograms). Extrapolating from release curves for these molecules (Figure 6E,G; see Methods), we estimated the total number of membrane binding events per unit area and time for anterior and posterior molecules. We found that during maintenance, single PAR-3(ΔCR1)::GFP molecules bound the anterior membrane 2.5 times more frequently than the posterior membranes in wild-type embryos and 2.0 times more frequently in *par-1(RNAi)* embryos (Figure 6F,H). Thus PAR-3 monomers bind membranes at higher rates where PAR-3 is already enriched, consistent with positive feedback on PAR-3 recruitment. Together, the A:P ratios in effective dissociation rate (3.8) and recruitment rate (~2) are sufficient to account quantitatively for the total PAR-3 asymmetry observed at late maintenance phase in *par-1* mutant embryos.

We then asked: If the observed membrane binding asymmetry reflects positive feedback on PAR-3 recruitment, is this feedback sufficiently strong to ensure dynamically stable PAR-3 asymmetries in the absence of posterior inhibition? We added a simple form of feedback to the model (cyan arrow in Figure 7A), in which the rate constant for monomer recruitment is given by:

$$k_{on} = \left(k_{basal} + k_f f(A)\right)$$

where k_{basal} is the rate constant for basal recruitment, $f(A)$ defines the form of positive feedback, and k_f tunes its strength. Because recruitment asymmetries of PAR-3 are similar in early and late maintenance phase, despite a nearly two-fold change in the anterior PAR-3 density, we assumed a simple form of saturating feedback governed by:

$$f(A) = \min\left(A, A^{(Sat)}\right)$$

where $A^{(Sat)}$ is the density of PAR-3 above which feedback saturates. To facilitate direct comparisons with experimental measurements, we defined a feedback strength as the ratio of the recruitment rate at the spatially uniform steady state to the basal recruitment rate:

$$S_{feedback} = \frac{k_f A^{(Sat)}}{k_{basal}}$$

With these assumptions, the model predicts one of two dynamical behaviors: either (a) no stably polarized state exists, (i.e. the spatially uniform steady state is always stable) or (b) spatially uniform and asymmetric stable states coexist, and a transient local depletion of PAR-3 can induce a transition from the spatially uniform to the polarized state, as observed during normal polarity establishment. We refer to this latter case as inducible polarity. As shown in the phase diagram in Figure 7B, the predicted dynamics depend on just two quantities: the mean oligomer size s, which measures the strength of positive feedback due to size-dependent oligomer dissociation and $S_{feedback}$, the strength of positive feedback on monomer recruitment defined above. The model predicts that both forms of feedback are required for stable inducible polarity

and identifies the combinations of feedback that would be sufficient to produce the stable PAR-3 asymmetry observed at steady state during maintenance phase.

To locate the maintenance phase embryo in this phase diagram, we parameterized the model by first assuming a reasonable target for A_h, the anterior steady state density of PAR-3 as a function of the total available density. We then chose a value $A^{(\mathrm{Sat})} < A_h$ for the saturation level, in accordance with our observation that feedback is saturated during maintenance phase. To fix the polymerization kinetics, we used our empirically measured values for k_{dep} and $k_{\mathrm{off}}^{(n)}$, then varied k_{pol} so that polymerization kinetics agreed with our experimental data. This left the two binding parameters k_{basal} and k_f, which we set to the unique values that reproduced the target steady state density A_h and A/P asymmetry in total PAR-3 density. The large magenta dot locates the model-predicted behavior within the phase diagram in Figure 7B for the inferred parameter values. This choice of parameters yielded a recruitment asymmetry within the range measured experimentally (Fig. 6H), providing evidence for the accuracy of our model. Importantly, the predicted value of feedback strength $\frac{k_f A^{(\mathrm{Sat})}}{k_{\mathrm{basal}}}$ was relatively insensitive to the exact choice of $A^{(Sat)}$ and A_h. This analysis reveals that for tightly constrained model parameters, the combined strength of feedback due to size-dependent oligomer dissociation and feedback on monomer recruitment is sufficient to endow the zygote with the ability to form dynamically stable PAR-3 asymmetries in response to a transient local input (pink dot in Figure 7B).

The asymmetric membrane binding of PAR-3(ΔCR1)::GFP is consistent with positive feedback of PAR-3 on its own recruitment (cyan arrow in Figure 7A). However, it could also reflect an asymmetric bias on monomer binding that does not depend on local densities of PAR-3 (orange

arrow in Figure 7A). To distinguish these two scenarios, we used simulations to predict how the PAR-3 asymmetry should vary with total PAR-3 levels (and thus mean oligomer size), given either a fixed asymmetric bias or positive feedback on recruitment. We then tested these predictions, by varying PAR-3 levels in living embryos (Figure 7C-E).

We found that a key difference between the two scenarios lies in the PAR-3 asymmetries predicted for low levels of total PAR-3 (compare cyan and orange curves in Figure 7E). For a fixed two-fold A:P bias in monomer binding, the predicted PAR-3 asymmetries persist as the total PAR-3 approaches 0, approaching a fixed value > 1.7 (orange curve in Figure 7E), which is determined by the combined effects of asymmetric recruitment and the negative dependence of effective dissociation rate on density of membrane-bound PAR-3. In contrast, for positive feedback on membrane recruitment whose strength yields a two-fold difference in recruitment rates at steady state, our simulations predict that PAR-3 asymmetries disappear entirely below a threshold level of PAR-3 (cyan curve in Figure 7E).

To distinguish these possibilities, we used RNAi against PAR-3 to systematically vary the total abundance of PAR-3 in the system. We used a strain expressing endogenously tagged PAR-3::GFP, allowing us to measure the total density of membrane associated PAR-3, the mean oligomer size, and the asymmetry in PAR-3 in late maintenance phase for each embryo (see Methods for details). We focused our analysis on embryos that established PAR-3 and we verified that loss of asymmetry during maintenance was not caused by redistribution of PAR-3 by cortical flow (Figure S3). We confirmed the predicted dependence of mean oligomer size on total density of membrane-bound PAR-3 (Figure 7D). More importantly, plotting the observed

PAR-3 asymmetry against mean oligomer size shows that the response to progressive depletion of PAR-3 strongly resembles, both qualitatively and quantitatively, the response predicted for the positive feedback scenario (Figure 7E). We conclude that asymmetric recruitment of PAR-3 to the cell membrane results from positive feedback, and that this positive feedback on recruitment, combined with positive feedback due to size-dependent dissociation of PAR-3 oligomers, is sufficient to support stable PAR-3 asymmetries during maintenance in embryos lacking posterior inhibition by PAR-1.

PAR-6/PKC-3 are required for positive feedback on PAR-3 recruitment and stable PAR-3 asymmetries.

Because the asymmetric recruitment of PAR-3 does not require an intact CR1 domain, positive feedback on recruitment must involve the interaction of PAR-3 with additional factors. The other anterior polarity proteins PAR-6, PKC-3 and CDC-42 are an attractive set of candidates. PAR-6 and PKC-3 form an obligate heterodimer that can bind directly to either PAR-3 or CDC-42 [43–50]. The PAR-6/PKC-3 heterodimer is thought to cycle between PAR-3-bound and CDC-42-bound states during polarization [16,39,51,52]. Although the bulk of PAR-6/PKC-3 is thought to be complexed with CDC-42 during maintenance phase, its local recruitment to the membrane requires both PAR-3 and CDC-42 [17,51], suggesting that PAR-6/PKC-3 interacts at least transiently with PAR-3. Therefore, we hypothesized that PAR-6/PKC-3, and perhaps CDC-42, might act as intermediaries to promote positive feedback on PAR-3 recruitment.

To evaluate this possibility, we examined the effects of depleting PAR-6 on PAR-3 asymmetries during polarization in *par-1* mutant and heterozygous control embryos. Consistent with previous

reports [11,16,53], PAR-3 oligomers accumulate on the membrane during polarity establishment phase in control (*par-1/+*) embryos depleted of PAR-6, although cortical flows and anterior enrichment of PAR-3 were significantly reduced (Figure 8A; *par-6(RNAi)*, Movie S6). However, these asymmetries were completely lost during maintenance phase. This loss of asymmetry was accompanied by both a rapid decrease in PAR-3 density and oligomer size on the anterior cortex, and by the rapid transport of PAR-3 oligomers towards the posterior pole by aberrant posterior directed cortical flows[17] (Figure 8A, Movie S6). However, co-depleting PAR-6 and MRCK-1 (which is required for cortical contractility and flow during mitosis[17,22]) produced a similarly rapid decrease in anterior oligomer size and complete loss of PAR-3 asymmetry during maintenance phase (Figure 8A,B; *par-6(RNAi);mrck-1(RNAi)* , Movie S6).

The decrease in PAR-3 density and oligomer sizes produced by depleting PAR-6/PKC-3 in *par-1* heterozygotes could be due to increased inhibition by PAR-1 [12], which accumulates uniformly in embryos lacking PAR-6 /PKC-3 [54]. However, depleting PAR-6 in *par-1* homozygous mutant embryos produced similarly rapid and complete loss of PAR-3 oligomers during maintenance phase (Figure 8C,D; *par-6(RNAi),* Movie S7). We also observed rapid decrease in PAR-3 density, oligomer size and overall PAR-3 asymmetry in *par-1* homozygotes co-depleted of PAR-6 and MRCK-1 relative to untreated *par-1* homozygotes, although the loss was incomplete at late maintenance phase (Figure 8C,D; *par-6(RNAi);mrck-1(RNAi*, Movie S7*)*). Altogether these data show that PAR-6/PKC-3 play a central role in maintaining PAR-3 asymmetries during maintenance phase independent of posterior inhibition by PAR-1 and cortical flow.

The changes in PAR-3 density and oligomer size induced by co-depleting PAR-6 and MRCK-1 could be caused by increased depolymerization or monomer dissociation, decreased recruitment rates, or both. Using single molecule imaging at low duty ratios as above (Figure 5E), we found there was no significant difference in depolymerization rates (k_{dep}) during early maintenance phase in PAR-6-depleted embryos compared to untreated controls (Figure 8E; Figure S4A). Similarly, comparing release curves for PAR-3(ΔCR1)::GFP suggests that there is no significant difference in the dissociation rates of monomeric PAR-3 in control vs *par-6(RNAi); mrck-1(RNAi)* embryos (Figure S4B,C). In contrast, the asymmetric recruitment of PAR-3(ΔCR1)::GFP during early maintenance phase was abolished in embryos co-depleted of PAR-6 and MRCK-1 (Figure 8F), even though endogenous PAR-3 is highly enriched on the anterior cortex during early maintenance phase in these embryos (Figure 8A,B). Thus PAR-6/PKC-3 stabilize PAR-3 asymmetries during maintenance phase by promoting asymmetric recruitment of PAR-3.

Finally, we used the empirically constrained model to assess whether the loss of PAR-3 recruitment asymmetry produced by co-depleting PAR-6 and MRCK is sufficient to explain the dynamic loss of PAR-3 asymmetries observed during maintenance phase in these embryos. We set $k_f = 0$ to mimic complete loss of asymmetric binding, and simulated PAR-3 dynamics from the initial distribution measured at late establishment phase in *par-1* homozygote embryos co-depleted of PAR-6 and MRCK (Figure 8C,D; *par-6(RNAi);mrck-1(RNAi)*). As expected from the phase diagram on Figure 7B, the model predicts the complete loss of asymmetry, but the time course is too slow to reach completion during maintenance phase, consistent with the incomplete loss of asymmetry observed at late maintenance phase in these embryos (Figure 8H). We

conclude that PAR-6/PKC-3 act as a key intermediary to support positive feedback of PAR-3 on its own recruitment and dynamically stable PAR-3 asymmetries.

CDC-42 promotes dynamically stable PAR-3 asymmetries by tuning basal rates of PAR-3 recruitment

We also assessed the consequences of depleting CDC-42 in *par-1* mutant and heterozygous control embryos. In *par-1* heterozygotes depleted of CDC-42, PAR-3::GFP asymmetries formed during polarity establishment phase and relaxed toward lower levels during maintenance phase, as observed in controls (Figure 8C*;* control, *cdc-42(RNAi)*, Movie S6), although overall density and mean oligomer size were slightly higher than in controls (Figure 8D; compare control and *cdc-42(RNAi)*). There was no significant difference in the depolymerization of full length PAR-3::GFP or dissociation of monomeric PAR-3(ΔCR1)::GFP relative to controls (Figure 8E, Figure S4D,E).

In contrast, asymmetric recruitment of PAR-3(ΔCR1)::GFP was reduced, but not abolished in embryos depleted of CDC-42 (Figure 8F), even though endogenous PAR-3 remains asymmetrically enriched during maintenance phase in these embryos, compared to controls (Figure 8A,B). In *par-1* homozygotes depleted of CDC-42, PAR-3:GFP became enriched during polarity establishment phase to slightly higher levels than observed in untreated homozygous controls, but these asymmetries were almost completely lost during polarity maintenance phase (Figure 8C,D; *cdc-42(RNAi)*, Movie S7). Strikingly, while loss of PAR-3 asymmetry in *par-6(RNAi);mrck-1(RNAi)* embryos is associated with a decrease in anterior PAR-3 density and

oligomer size, the loss of asymmetry in *cdc-42(RNAi)* embryos was associated with an increase in posterior PAR-3 density and oligomer size (Figure 8D; *cdc-42(RNAi)*, Movie S7).

The observation that posterior densities and oligomer sizes increase, while anterior densities and oligomer sizes remain the same in embryos depleted of CDC-42 suggest that the reduced asymmetry is primarily due to an increase in the basal recruitment rate k_{basal}, which would cause a decrease in the overall feedback strength measured by $S_{feedback} = \frac{k_f A^{(Sat)}}{k_{basal}}$. To test this possibility, we modified our model by reducing k_{basal} to 50% of the control value while holding k_f constant to approximate the recruitment asymmetry measured in CDC-42-depleted control embryos. Then we simulated PAR-3 dynamics from the initial distribution measured at late establishment phase in *par-1* homozygote embryos depleted of CDC-42 (Figure 8C,D; *cdc-42(RNAi)*). The simulations reproduced the qualitative signature and time course of PAR-3 asymmetry loss observed in CDC-42-depleted embryos in which anterior PAR-3 levels fall toward and posterior levels rise toward an intermediate spatially uniform level (Figure 8H). Again, the loss of asymmetry was incomplete at late maintenance phase, as observed experimentally (Figure 8H).

In summary, these data show that both PAR-6/PKC-3 and CDC-42 are required for dynamically stable PAR-3 asymmetries in the absence of posterior inhibition by PAR-1, but the data suggest that PAR-6/PKC-3 and CDC-42 act in different ways: PAR-6/PKC-3 is required for positive feedback on PAR-3 recruitment, while CDC-42 reduces basal rates of recruitment, which increases the overall strength of positive feedback.

Discussion

Two feedback loops encode robust self-stabilizing unipolar PAR-3 asymmetries

Studies of PAR-mediated polarity have focused on how mutual antagonism between two sets of PAR proteins drive their stable enrichment in complementary cortical domains [12,17,23,55–58]. However, the ability of PARs to form and stabilize *unipolar* asymmetries has remained poorly understood [29–33]. Here we have combined single molecule analysis with mathematical modeling and experimental perturbations to identify two positive feedback loops that synergistically ensure robust dynamically stable unipolar PAR-3 asymmetries in *C. elegans* zygotes. First, the intrinsic dynamics of PAR-3 membrane binding, oligomerization, and size-dependent oligomer dissociation encode negative feedback on PAR-3 dissociation. Second, PAR-3 acts indirectly to promote its own recruitment through a mechanism that depends on its conserved binding partners PAR-6 and PKC-3. We have shown that these two modes of positive feedback are individually necessary and jointly sufficient to account, quantitatively, for the locally inducible and dynamically stable PAR-3 asymmetries observed in zygotes lacking posterior inhibition by PAR-1. Thus, a tight correspondence between model-predicted and observed dynamics, integrating multiple independent measurements of single molecule kinetics, oligomer size distributions and the time evolution of cell-scale asymmetries, reveals a robust, internally self-consistent and quantitively accurate picture of how self-stabilizing unipolar PAR-3 asymmetries emerge from molecular scale kinetics.

Intrinsic dynamics of membrane binding and oligomerization encode nonlinear positive feedback on PAR-3 accumulation

Self-oligomerization is a conserved feature of PAR-3 [34] Recent studies in *C. elegans* zygotes have emphasized how this property can contribute to the advective transport of PAR-3 (and its binding partners PAR-6/PKC-3) during symmetry-breaking, through increased physical coupling to the cortical actomyosin cytoskeleton and through increased residence time via size-dependent binding avidity [17,26,39–41]. Here we have shown that the intrinsic dynamics of membrane binding and oligomerization also confer non-linear positive feedback on PAR-3 accumulation. Combining single molecule analysis and kinetic modeling, we find that three processes account quantitatively for the distribution of PAR-3 oligomers, and the time scale of approach to steady state during maintenance phase: fast monomer binding ($k_{off} = \sim 3\ sec$), slower oligomerization ($k_{dep} = \sim 0.1\ sec$), and even slower size-dependent dissociation of PAR-3 oligomers. Our model predicts, and our experiments confirm, a positive dependence of mean oligomer size on density, and we have measured a sharp decrease in oligomer dissociation rate with size. Together these make the average rate constant for PAR-3 dissociation a sharply non-linear function of PAR-3 density. For measured kinetic parameters, we find that this negative feedback on PAR-3 dissociation contributes a nearly 4-fold A:P difference in the flux of PAR-3 molecules off the membrane, accounting for half the total asymmetry observed in *par-1* mutant embryos lacking posterior inhibition of PAR-3.

Importantly, non-linear feedback on dissociation is a generic consequence of reversible membrane binding and oligomerization. In this simple generic form, it does not consume energy, and therefore it cannot alone sustain dynamically stable asymmetries. However, it can sharply reduce the amount of additional energy-consuming feedback needed for stable asymmetries. Because weak membrane binding and self-oligomerization are widespread and

easily evolved properties of proteins, we expect that many types of cells use this form of feedback to promote symmetry-breaking and stable polarity. Indeed, our results add to a growing body of work emphasizing the importance of clustering/oligomerization of peripheral membrane binding proteins to establishment and maintenance of cell surface asymmetries in polarized cells[17,59–61].

PAR-6/PKC-3 mediate positive feedback on PAR-3 recruitment

Our observations suggest that the additional feedback required for dynamically stable PAR-3 asymmetries come from positive feedback on PAR-3 monomer recruitment. First, monomeric PAR-3(ΔCR1)::GFP binds at > 2-fold higher rates to anterior membranes where PAR-3 itself is enriched. In principle this binding asymmetry could reflect either a fixed PAR-3-independent bias, or positive feedback on monomer recruitment. However, comparing model variants tightly constrained by our experimental measurements can cleanly distinguish these possibilities. A model based on fixed bias cannot explain the observed dependence of PAR-3 asymmetry on total PAR-3 density, while a model based on simple feedback can and does for experimentally measured parameters.

Our data suggest that the other aPARs play central roles in mediating (PAR-6/PKC-3) or tuning (CDC-42) positive feedback on PAR-3 recruitment. Co-depleting PAR-6 and MRCK-1 (to prevent aberrant cortical flows) in *par-1* mutants leads to rapid loss of PAR-3 asymmetry during maintenance phase, from an initially polarized state. This loss is not due to changes in depolymerization or monomer dissociation rates; instead, co-depleting PAR-6 and MRCK-1 completely blocks the asymmetric recruitment of PAR-3(ΔCR1)::GFP, even though endogenous

full-length PAR-3 remains highly asymmetric in these embryos. Thus PAR-6/PKC-3 are required for positive feedback on PAR-3 monomer recruitment and dynamically stable unipolar PAR-3 asymmetries in the absence of posterior inhibition by PAR-1. Depleting CDC-42 in *par-1* mutant embryos also leads to loss of PAR-3 asymmetries, but through an increase in basal rates of PAR-3 monomer recruitment and aberrant posterior accumulation of PAR-3. In both cases, changing a single quantity – the strength of positive feedback on recruitment – allows the model predicts correctly the mode and time course of asymmetry loss observed in experiments.

The mechanism(s) by which PAR-6/PKC-3 and CDC-42 mediate positive feedback on PAR-3 recruitment remain unclear, but previous studies and our data constrain the class of possible mechanisms. PAR-3 asymmetries persist during maintenance phase in *par-1;chin-1* double mutant embryos in which CDC-42 activity, PAR-6 and PKC-3 are uniformly enriched [17]. Thus, positive feedback does not require the asymmetric enrichment of PAR-6/PKC-3 or active CDC-42. Instead, these data favor a mechanism in which a transient interaction of PAR-6/PKC-3 with PAR-3 oligomers licenses their ability to recruit additional PAR-3 monomers from the cytoplasm. A similar mechanism was previously proposed for positive feedback on GTPase activation by Anillin [62].

PAR-6/PKC-3 heterodimers can form distinct ternary complexes with PAR-3 and active CDC-42[16,51,52]. PAR-3 and CDC-42 compete for binding to PAR-6/PKC-3 in vitro [63]; PAR-6/PKC-3 dimers are thought to cycle between PAR-3 and CDC-42-bound states in vivo [16], and binding to both PAR-3 and CDC-42 is required for localization of PAR-6/PKC-3 during maintenance phase in C. elegans zygotes [17,51]. Thus, one possibility is that PAR-6/PKC-3 heterodimers act as a

shuttle – cycling between PAR-3 and CDC-42 bound states; In particular, CDC-42 may bind and displace PAR-6/PKC-3 when it is bound to PAR-3 and cytoplasmic PAR-3 monomers may bind and displace PAR-6/PKC-3 when it is bound to CDC-42. For this to work, an enzymatic step would be required to toggle the relative affinities of PAR-6/PKC-3 for CDC-42 and PAR-3, but since both PAR-3 and CDC-42 are both direct phosphorylation substrates of PKC-3 [64,65], there are multiple ways in which this mechanism could work. One caveat is that this scenario does not explain why depleting CDC-42 leads to increased basal rates of PAR-3(ΔCR1)::GFP binding.

An alternative scenario is that PAR-6/PKC-3 dimers bound to PAR-3 could recruit a second PAR-3 molecule. Strong binding of PAR-6/PKC-3 to PAR-3 in vitro, and membrane recruitment of PAR-6/PKC-3 *in vivo* requires direct binding between a PDZ-binding motif (PBM) on PKC-3 and the PDZ2 domain of PAR-3 [50]. However, a PAR-6/PKC-3 heterodimer can also bind PAR-3 via PAR-6 [48], or through an interaction between the kinase domain of PKC-3 and PAR-3 [50,66]. Thus, in principle, PAR-6/PKC-3 heterodimers complexed with PAR-3 at the membrane could recruit additional molecules of cytoplasmic PAR-3. For this to constitute positive feedback, an energy consuming step (e.g phosphorylation of PAR-3 by PKC-3) would be required. Moreover, the fast mobilities of newly-bound PAR-3(ΔCR1)::GFP molecules imply that their asymmetric recruitment does not require direct stable binding to existing PAR-3 oligomers. Thus, a bridging mode of recruitment would have to be very transient, delivering cytoplasmic monomers into a freely diffusing membrane-bound state, or it would have to preference the use of membrane-bound PAR-3 monomers over oligomers. Distinguishing these and other possible mechanisms for PAR-6/PKC-3 mediated feedback on PAR-3 monomer recruitment will be an important goal for future work.

PAR-3 is the keystone member of the PAR polarity network, which is required for all other PAR asymmetries. In the *C. elegan*s zygote, PAR-3 is the only member that remains asymmetric when all other known members of the PAR network are absent or symmetrically distributed [17]. In the *C. elegans* zygote, and other cells, the spatial distribution of PAR-3 determines where PAR-6/PKC-3 load onto the membrane and into a complex with active CDC-42, to form a gradient of PKC-3 activity that defines anterior (or apical) identity and opposes posterior (or basolateral) identity [16,17,67]. Thus, the spatial distribution of PAR-3 dictates polarity, even in cells where mutual inhibition plays an important role

Our analysis of a model tightly constrained by empirical measurements reveals that the combination of negative feedback on PAR-3 dissociation and positive feedback on PAR-3 recruitment encodes the co-existence of two dynamically stable states: a spatially uniform state with high PAR-3 levels as observed during maintenance phase in unpolarized zygotes lacking a functional sperm cue; and a polarized state with high anterior and low posterior levels of PAR-3, matching those observed during maintenance phase in polarized zygotes. Importantly, the model predicts that local depletion of PAR-3, mimicking the effects of cortical flow or local PAR-1 accumulation during zygotic symmetry breaking [11,12], can induce an irreversible transition from the spatially uniform to the stably polarized state. Thus, the intrinsic kinetics of PAR-3 membrane-binding and oligomerization, plus weak feedback on PAR-3 recruitment mediated by PAR-6/PKC-3, endow *C. elegans* zygotes with a robust symmetry-breaking response to the sperm cue, independent of mutual antagonism. Because these core features of PAR-3 and its interactions with PAR-6/PKC-3 are conserved across the metazoa, it seems likely that they may

contribute to stabilizing unipolar asymmetries observed in other contexts, for example in neuroblasts [27,31], or meiotic oocytes[68] , and that they may play key roles in controlling PAR asymmetries, even in cells like the *C. elegans* zygote that also rely on mutual inhibition.

Acknowledgments

This work was funded by NIGMS grants T32 GM007197 and 1R01GM098441.

Declaration of interests

The authors declare no competing interests

Supplemental information

Modeling supplement

Supplemental Figures S1-5

Supplemental Movies S1-7

Figure Legends

Figure 1. PAR polarity in the *C. elegans* embryo. (A) Schematic illustrating key interactions that maintain PAR asymmetries in the *C. elegans* zygote. On the left, PAR-3 promotes entry of the PAR-6/PKC-3 dimer into a complex with active CDC-42. Within this complex, PKC-3 inhibits cortical accumulation of posterior PARs. PAR-1 inhibits cortical accumulation of PAR-3, while CHIN-1 inhibits CDC-42 activity. **(B)** In embryos lacking posterior inhibitors PAR-1 and CHIN-1, CDC-42, PAR-6 and PKC-3 are uniformly distributed at the membrane, and all posterior PARs are absent or uniformly cytoplasmic. Nevertheless, PAR-3 oligomers remain asymmetrically distributed.

Figure 2. PAR-3 asymmetries approach a steady state during mitosis despite rapid continuous turnover. (A) Individual near-TIRF images from a time-lapse sequence showing PAR-3 oligomer intensities and distributions at the cell surface in homozygous *par-1* mutant embryos at early establishment, late establishment and late maintenance phase. **(B-D)** Results of particle detection analysis showing **(B)** mean oligomer size, **(C)** oligomer density, and **(D)** total PAR-3 fluorescence density over time on the anterior (magenta) and posterior (blue) membrane in homozygous *par-1* mutant embryos. Data are from n = 12 embryos aligned with respect to the onset of maintenance phase. The grey shaded area indicates maintenance phase. Solid lines indicate the mean and dots indicate S.E.M. at each time point. **(E)** Representative micrographs showing the time course of recovery of PAR-3::GFP in the anterior domain after photobleaching the entire field of view in an embryo in early maintenance phase. Timestamps indicate seconds after photobleaching. Orange arrowheads indicate individual PAR-3 oligomers that persist during recovery. **(F)** Plots of average fluorescence density vs time before and after photobleaching, normalized to prebleach levels and corrected for the overall decrease in fluorescence observed during maintenance phase (see Methods). Error bars indicate SEM (n = 4 embryos). **(G)** Box plot showing time to half maximal recovery ($t_{1/2}$) after photobleaching.

Figure 3. PAR-3 oligomer size distributions reflect kinetics of membrane binding and polymerization. (A) A simple kinetic model for PAR-3 oligomerization dynamics. Monomers bind reversibly to the membrane with rate constants k_{on} and k_{off}. Membrane-bound monomers bind oligomers with rate constants k_{pol} and k_{dep}, and oligomers dissociate from the membrane with size-dependent rate constant $k_{off}(n)$ where n is the number of subunits in the oligomer.

We neglect direct binding of cytoplasmic monomers to membrane bound oligomers and membrane binding of oligomers with size n > 1 (see text for justification). **(B)** Predicted steady state distribution of oligomer sizes $A_n = A_1\alpha^{n-1}$ for different values of oligomerization strength α (see text for details) **(C)** Micrographs showing distributions of PAR-3 before (left panel) and after 30 seconds of continuous laser exposure at full power (right panel) in late maintenance phase *par-1* mutant embryos. Dashed orange and green outline the regions in which anterior and posterior measurements were made. **(D)** Distributions of anterior (orange) and posterior (green) speckle intensities measured in a representative embryo. **(E)** Distributions of speckle intensities after photobleaching (gray) in the same embryo. **(F)** Inferred distributions of PAR-3 oligomer sizes on the anterior and posterior cortex of a representative embryo, based on calibrating raw intensities to the estimated intensity distribution of single molecules. Dashed lines indicate data fit to the equation $A_n = A_1\alpha^{n-1}$. **(G)** Estimates of oligomerization strength α (left) and mean oligomer size s (right) on the anterior and posterior of n = 8 individual embryos in late maintenance phase.

Figure 4. Size-dependent dissociation of PAR-3 oligomers induces negative feedback on average rates of PAR-3 dissociation.

(A) Representative micrograph of a maintenance phase embryo expressing endogenously-tagged mNeonGreen::PAR-3 and depleted of myosin II heavy chain NMY-2 by RNAi. **(B)** Individual trajectories (yellow traces) for all oligomers detected in the first movie frame. **(C)** Estimated rate constants for dissociation rates of PAR-3 oligomers from the membrane as a function of inferred

number of subunits n. Error bars represent the SEM. Data were compiled from n = 3 individual embryos.

(D) Overlay of the distributions of background-subtracted intensities of (blue) newly detected PAR-3::GFP speckles from the data in (A) and (peach) single molecule speckles after photobleaching in the same cells. **(E)** Predicted dependence of the effective rate constant for PAR-3 dissociation $k_{effective} = \frac{\sum_{n=1}^{\infty} k_{off}(n) n\alpha^{n-1}}{\sum_{n=1}^{\infty} n\alpha^{n-1}}$ on the total density of membrane-bound PAR-3, normalized to anterior density at steady state (see Methods for details).

Figure 5. Membrane unbinding and depolymerization set the timescale for slow approach to steady state distributions of PAR-3 during maintenance phase

(A) Representative image showing single molecules of PAR-3::GFP imaged at high laser power and short exposure times to ensure accurate tracking of fast diffusing molecules. **(B)** (left) Schematic illustrating the scheme for constructing release curves. (right) Release curves measured for single molecules of PAR-3::GFP on the anterior and posterior cortex of wild type embryos under continuous illumination. Thin traces show release curves for individual embryos (n = 8); Thick traces show data summed for all embryos. Data were normalized by total numbers of anterior tracks. **(C)** Distributions of root mean square displacements after 200 msec ($RMSD_{200}$) for anterior (orange) and posterior (green) molecules pooled from 8 embryos. Plots on the right show reference RMSD@200 distributions for (cyan) tracked PAR-3 oligomers (n = 7 embryos) and (magenta) simulated Brownian diffusion with diffusivity D = 0.1 μm^2/sec. In middle panel, the blue curve shows a weighted (60/40) sum of RMSD@200 distributions for oligomers and for simulated diffusion. **(D)** Release curves for PAR-3::GFP molecules imaged with fixed laser power and exposure times but different duty ratios. Each curve represents the

sum of data from multiple embryos: (Duty ratio = 1, n = 7; Duty ratio = 0.2; n = 7, Duty ratio = 0.1; n = 12; Duty ratio =, n = 13). **(E)** Disappearance rate constants (k_{obs}) measured for different duty ratios by fitting the linear portions of the release curves (see Methods for details). The dashed line represents a linear least-squares fit of the data to the equation $k_{obs} = k_{dep} + k_{pb} * dr$. **(F)** Estimates of k_{off} from streaming data for full length PAR-3::GFP (n = 9 embryos) and oligomerization defective PAR-3(ΔCR1)::GFP (n = 11 embryos). **(G)** Comparison of measured (blue curve) approach to steady state and the simulated approach (dashed red curve) given measured values for $k_{off}(n)$ and k_{dep}.

Figure 6. Asymmetric recruitment of PAR-3 monomers underlies maintenance of PAR-3 asymmetries.

(A,B) Distribution of single molecule appearance events for oligomerization-defective PAR-3(ΔCR1)::GFP in representative **(A)** control and **(B)** *par-1(RNAi)* embryos, detected by single molecule imaging. Each dot represents a single binding event. **(C-E)** RMSD@200 distributions **(C)**, release curves **(D)**, and estimates of recruitment asymmetry **(E)** measured from pooled single molecule trajectories for n = 6 control embryos. **(F-H)** RMSD@200 distributions **(F)**, release curves **(G)**, and estimates of recruitment asymmetry **(H)** measured from pooled single molecule trajectories for n = 7 *par-1(RNAi)* embryos.

Figure 7. Positive feedback on PAR-3 monomer recruitment and size-dependent dissociation of oligomers, are both necessary and sufficient to stabilize PAR-3 asymmetries.

(A) Modified versions of the reaction diagram in Figure 3A, showing two alternative assumptions for the mechanism that underlies asymmetric recruitment: (blue arrow): Membrane-

bound PAR-3 feeds back to promote recruitment of PAR-3 monomers to the membrane. (orange arrow): A fixed asymmetric input, whose strength is independent of PAR-3 densities, biases recruitment to the anterior cortex. **(B)** Phase plane derived for the version of the model with positive feedback on membrane recruitment, showing how the ability to polarize depends on mean oligomer size and feedback strength (see text for details). Experimental measurements of mean oligomer size and feedback strength in the *C. elegans* zygote place PAR-3 in the region of phase space where polarization is possible (large magenta dot). **(C)** Schematic illustrating the PAR-3 depletion experiment. Total pool of PAR-3 can be tuned by varying feeding time on RNAi plates. **(D)** Scatter plot showing the relationship between mean oligomer size and total membrane-bound PAR-3 measured across increasing levels of PAR-3 RNAi depletion. Solid curve shows a fit of the data to model prediction. **(E)** Scatter plot showing the relationship between mean oligomer size and PAR-3 asymmetry during late maintenance phase. Filled dots represent embryos where polarity was established by late interphase and unfilled dots represent embryos where polarity was not established. The magenta curve represents the predicted relationship for the model in which asymmetric recruitment is the result of a cryptic bias and the cyan line represents the prediction of a model where it is the result of saturating positive feedback (see text for details).

Figure 8. CDC-42 and PAR-6/PKC-3 reinforce PAR-3 asymmetries during maintenance phase by promoting asymmetric recruitment of PAR-3 (A) Representative micrographs showing PAR-3 oligomer sizes and distribution during maintenance phase in *par-1* heterozygote (*par-1/+*) embryos for the indicated RNAi depletions. Top and bottom micrographs show the distribution of PAR-3 oligomers in early (-240 sec) and late (0 sec) maintenance phase. Time is

measured relative to the point where anterior density of PAR-3 reached a minimum in late maintenance phase (see Methods for details). Kymographs show how the distribution changes over the 240 seconds between these time points. Diagonal streaks in the kymographs indicate transport of PAR-3 oligomers by cortical flow. **(B)** Corresponding plots of total fluorescence density of PAR-3 within segmented speckles during maintenance phase. Bold lines indicate the mean and red dots indicate the standard error of the mean across individual embryos (control: n = 8, *cdc-42(RNAi)*: n = 7, *par-6(RNAi):* n = 6, *par-6(RNAi)*; *mrck-1(RNAi*): n = 8). **(C)** Representative micrographs showing PAR-3 oligomer sizes and distribution during maintenance phase in *par-1* homozygous (*par-1/par-1*) embryos for the indicated RNAi depletions. Data are presented as described in **(A)**. **(D)** Corresponding plots of total fluorescence density of PAR-3 within segmented speckles during maintenance phase. Bold lines indicate the mean and red dots indicate the standard error of the mean across individual embryos (control: n = 10, *cdc-42(RNAi)*: n = 6, *par-6(RNAi):* n = 9, *par-6(RNAi)*; *mrck-1(RNAi*): n = 14). **(E)** Estimates of depolymerization rates (k_{dep}) in wild type (n = 8), *cdc-42(RNAi)* (n = 12) and *par-6(RNAi)* (n = 14) embryos expressing transgenic PAR-3::GFP. **(F)** Boxplots showing A:P ratio of rates (#/unit area) for binding of oligomerization-defective PAR-3 molecules to the cell membrane in control (n = 6) and *par-6(RNAi)*; *mrck-1(RNAi*) (n = 6) embryos in early maintenance phase. **(G)** Boxplots showing A:P ratio of rates (#/unit area) for binding of oligomerization-defective PAR-3 molecules to the cell membrane in control (n = 6) and *cdc-42(RNAi)* (n = 6) embryos in late maintenance phase. **(H)**. Simulations showing predicted changes in anterior and posterior PAR-3 densities during maintenance phase starting from the initial distributions observed at the onset of maintenance phase. Left panel: Control conditions; Middle panel: Feedback strength set to

zero to mimic *par-6(RNAi)*; *mrck-1(RNAi*); Right panel: basal recruitment rate and feedback strength adjusted to mimic *cdc-42(RNAi).*

Supplementary Figure S1 (related to Figure 2) PAR-3 oligomer dynamics during maintenance phase in wild-type and *spd-5(RNAi)* embryos. (A) Individual near-TIRF images from a time-lapse sequence showing PAR-3 oligomer intensities and distributions at the cell surface in control (*par-1* heterozygote) embryos at early establishment, late establishment and late maintenance phase. **(B-D)** Results of particle detection analysis showing **(B)** mean oligomer size, **(C)** oligomer density, and **(D)** total PAR-3 fluorescence density over time on the anterior (magenta) and posterior (blue) cortex in control embryos. Data are from n = 8 embryos aligned with respect to the onset of maintenance phase. The grey shaded area indicates maintenance phase. Solid lines indicate the mean and dots indicate SEM. at each time point. **(E)** Individual near-TIRF images from a time-lapse sequence showing PAR-3 oligomer intensities and distributions at the cell surface in *spd-5(RNAi)* embryos at early establishment, late establishment, and late maintenance phase. **(F-H)** Results of particle detection analysis showing **(F)** mean oligomer size, **(G)** oligomer density, and **(H)** total PAR-3 fluorescence density over time on the cortex. Data are from n = 6 embryos aligned with respect to the onset of maintenance phase. The grey shaded area indicates maintenance phase. Solid lines indicate the mean and dots indicate SEM. at each time point.

Supplementary Figure S2 (related to Figure 4 and 6). Single molecule measurements of PAR-3::GFP and PAR-3(CR1)::GFP. (A-B) Plots of RMSD distributions and release curves for single molecules of PAR-3::GFP in *par-1* heterozygotes. **(A)** Distributions of root mean square

displacements after t = 200 msec ($RMSD_{200}$) measured for molecules tracked on the anterior and posterior cortex in n = 8 embryos. Each column represents data obtained using a different integrated intensity threshold for detecting single molecules, as indicated by the value for intensity threshold. Dark curve indicates simulated $RMSD_{200}$ distributions for molecules undergoing Brownian diffusion with diffusivity = 0.1 μm^2/sec. **(B)** Release curves measured for single molecules of PAR-3::GFP on the anterior and posterior cortex of wild type embryos under continuous illumination fort different feature detection thresholds. Thin traces show release curves for individual embryos (n = 8); Thick traces show data summed for all embryos. Data were normalized by total numbers of anterior tracks. **(C-D)** Plots of RMSD distributions and release curves for single molecules of PAR-3(ΔCR1)::GFP in *par-1* heterozygotes. **(C)** Distributions of root mean square displacements after t = 200 msec ($RMSD_{200}$) measured for molecules tracked on the anterior and posterior cortex in n = 9 embryos. Each column represents data obtained using a different integrated intensity threshold for detecting single molecules, as indicated by the value for feasturre detection threshold. Dark curve indicates simulated $RMSD_{200}$ distributions for molecules undergoing Brownian diffusion with diffusivity = 0.1 μm^2/sec. **(D)** Release curves measured for single molecules of PAR-3::GFP on the anterior and posterior cortex of wild type embryos under continuous illumination fort different feature detection thresholds. Thin traces show release curves for individual embryos (n = 9); Thick traces show data summed for all embryos. Data were normalized by total numbers of anterior tracks.

Supplementary Figure S3 (related to Figure 5). Examples of different phenotype classes in the PAR-3 depletion experiment shown in Figure 5D-E. Top and bottom micrographs show the distribution of PAR-3 at early and late maintenance respectively. We observed three distinct

classes: (left) polarity established and maintained, (middle) polarity established and not maintained and (right) polarity never established. For the middle class, the kymograph confirms that the loss of PAR-3 asymmetry was not due to redistribution of PAR-3 by posterior-directed cortical flows.

Supplementary Figure S4 (related to Figure 8). Mobilities and release curves for single molecules of PAR-3::GFP in control, *cdc-42(RNAi)* and *par-6(RNAi)* embryos. (A) Release curves for single molecules of transgenic PAR-3::GFP measured in control, *cdc-42(RNAi)* and *par-6(RNAi)* embryos during maintenance phase using high laser power, short exposures and low duty ratios to achieve accurate tracking with low photobleaching. All data were collected under identical conditions. Each thin curve represents data from a single embryo. Thick curves represent the average over (control: n = 8), (*cdc-42(RNAi)*: n = 12) and (*par-6(RNAi)*: n = 14) embryos. (**B-C**) Distributions of root mean square displacements after 200 msec (RMSD_200) and release curves for anterior (orange) and posterior (green) single molecules measured in (**B**) control and (**C**) *par-6(RNAi); mrck-1(RNAi)* embryos measured in early maintenance phase. (**D-E**) Distributions of root mean square displacements after 200 msec (RMSD_200) and release curves for anterior (orange) and posterior (green) single molecules measured in (**D**) control and (**E**) *cdc-42(RNAi)* embryos measured in late maintenance phase.

Supplemental Movie Legends

Movie S1. Dynamics of endogenously-tagged PAR-3 during polarity establishment and maintenance phases. Left: embryo from *par-1* heterozygote mother; Middle: Embryo from *par-1* homozygote mother; Right: *spd-5(RNAi)* embryo. All three embryos were imaged under

identical conditions. Time is measured relative to the onset of maintenance phase. Time compression 90:1

Movie S2. Dynamics of FRAP recovery. Embryo was subjected to photobleaching just before time 0. Time compression 18:1.

Movie S3. Fast imaging of endogenously-tagged PAR-3::GFP in an embryo depleted of myosin II heavy chain (*nmy-2(RNAi)*). Time compression 1:1.

Movie S4. Single molecule imaging of endogenously-tagged PAR-3::GFP and transgenic ΔCR1 PAR-3::GFP. (Left) endogenously-tagged PAR-3::GFP; (right) transgenic ΔCR1 PAR-3::GFP. Data were collected in streaming mode with 100% laser power at 15 frames per second to measure short-term mobilities and monomer dissociation rates. Time compression 2:1.

Movie S5. Single molecule observations of appearance events in control and *par-1(RNAi)* embryos expressing transgenic ΔCR1 PAR-3::GFP. (left) Control; (right(par-1(RNAi). Data were collected with intermediate laser power in streaming mode at 20 frames per second. Time compression 1:1.

Movie S6. Distribution of endogenously-tagged PAR-3::GFP oligomers during maintenance phase in embryos from *par-1*/+ mothers subjected to the indicated RNAi

depletions. Time is measured relative to the onset of maintenance phase. Time compression: 90:1

Movie S7. Distribution of endogenously-tagged PAR-3::GFP oligomers during maintenance phase in embryos from *par-1*/*par-1* mothers subjected to the indicated RNAi depletions. Time is measured relative to the onset of maintenance phase. Time compression: 90:1

STAR Methods

C. elegans culture and RNAi

We cultured *C. elegans* strains under standard conditions [69] on 60mm petri plates containing *E. coli* bacteria (OP50) raised on normal growth medium (NGM). Table 1 provides a list of strains used in this study. Unless otherwise specified, strains were provided by the Caenorhabditis Genetics Center, which is funded by the National Center for Research Resources.

Table 1. *C. elegans* strains used in this study.

Name	Genotype	Origin
Em267	par-3(it298[PAR-3::GFP]) III	Kenneth Kemphues
Em292	par-3(it298[PAR-3::GFP]) III; rol-4(sc8) par-1(it0051) V/DnT1 IV;V	Kenneth Kemphues
Em307	itIs268[ppar-3::PAR-3(V80D D198K)::GFP + unc-119(+)]; unc-119(ed3) III #5	Kenneth Kemphues
Em327	*par-6(cp60[par-6::mKate2::3xMyc + LoxP unc-119(+) LoxP]) I par-3(cp54[mNG::3xFlag::par-3]) III;*	Daniel Dickinson

We performed RNAi experiments using the feeding method [70]. We obtained bacteria targeting *par-1*, *par-3*, *par-6*, *cdc-42*, *mrck-1*, *spd-5*, and *nmy-2* from the Kamath RNAi library [71], and bacteria targeting GFP from Jeremy Nance. Briefly, we grew bacteria to log phase in LB with 50µg/ml ampicillin, seeded ~300µl of culture onto NGM plates supplemented with 50µg/ml ampicillin and 1mM IPTG, incubated plates at room temperature for two days, and then stored them at 4˚C for up to one week before use. We transferred L4 larvae or young adults (for *par-3(RNAi*)) to feeding plates and then cultured them at 25˚C before imaging as follows: 0 - 8 hours at 25˚C for *par-3(RNAi*) and 24 – 48 hours at room temperature (21-23˚C) for all others, adjusting exposure time to achieve the desired phenotype. We verified strong depletions of SPD-5 by observing complete failure of polarity establishment, strong depletions of PAR-6 and CDC-42 by observing symmetric first and second cleavages, and strong depletions of NMY-2 and MRCK-1 by observing absence of cortical flows during polarity establishment and/or maintenance phases.

Live imaging

For single molecule imaging experiments, we mounted embryos in egg salts containing ~21 μm diameter polystyrene beads. For all other experiments, we mounted embryos in eggs salts on agarose pads.

For data reported in Figures 3, 4, 5D-F, 6, 7, S2, S4, and S5, we used an Olympus IX50 inverted microscope equipped with an Olympus OMAC two-color TIRF illumination system, a CRISP autofocus module (Applied Scientific Instrumentation), and a 1.49 NA oil immersion TIRF objective. Laser illumination at 488 nm from a 50-mW solid-state Sapphire laser (Coherent) was delivered by fiber optics to the TIRF illuminator. We magnified images by 1.6x and collected

them on an Andor iXon3 897 EMCCD camera, yielding a pixel size of 100 nm. Image acquisition was controlled by Andor IQ software. For the data reported in Figures 2, 5A-C&G, 8, S1 and S3, we used a Nikon Ti2-E inverted microscope equipped with a LunF XL laser combiner housing solid state 488nm, 561nm and 640nm lasers and feeding three separate TIRF illumination arms, a Ti2 N-ND-P Perfect Focus unit, and a CFI APO 100X 1.49NA TIRF lens. We magnified images by 1.5X and collected them on an Andor IXON Life 897 EM-CCD camera to achieve a pixel size of ~106nm. Image acquisition was controlled by Nikon Elements software.

For all experiments, we used near-TIRF illumination. We set the laser illumination angle to standard values that we chose empirically to approximately maximize signal-to-noise ratio while maintaining approximately even illumination across the field of view. All embryos were oriented with their AP axis perpendicular to the axis of TIRF illumination to avoid any confounding effects of illumination gradients in comparisons of anterior vs posterior PAR-3 dynamics. Further details of the imaging conditions used for specific quantitative analyses appear below.

Image analysis

We performed particle detection and tracking as previously described [15,17]. Briefly, we used a slightly modified Matlab implementation (http://people.umass.edu/kilfoil/ downloads.html) of methods introduced by Crocker and Grier [72] to detect diffraction-limited features of interest as local intensity peaks in bandpass filtered images and then to determine their centroids and background-subtracted integrated intensities. We use μTrack software (http://github.com/DanuserLab/u-track) developed by Jaqaman and colleagues [73] to track features

over time. We integrated particle detection and tracking and all subsequent analyses using custom MATLAB scripts that are available upon request.

Timelapse analysis of PAR-3 oligomer dynamics

We measured PAR-3 oligomer dynamics in a *par-1* mutant strain expressing a C-terminal fusion of GFP to PAR-3 from the endogenous locus (hereon *par-1*; PAR-3::GFP), using *par-1/+* heterozygotes as controls. We collected images using near-TIRF illumination in timelapse mode using 10% laser power and 50msec exposure times at 3 sec intervals to minimize photobleaching. For each embryo and each timepoint, we identified PAR-3 clusters within hand-drawn anterior and posterior regions of interest (ROIs). For this and all subsequent measurements of feature intensities, we measured background-subtracted intensities by measuring integrated intensity within a circular ROI with radius of 3 pixels (300 nm) around the feature's centroid position and using the mean intensity within an annulus of width 2 pixels surrounding the central ROI to estimate local background. We then determined the minimal polygon containing all detected features and used its area to compute the densities of features or total PAR-3 fluorescence. For *spd-5(RNAi)* embryos, we used a single ROI for all measurements. For individual embryos, we plotted the smoothed mean intensities vs time to determine the timepoint in late establishment phase when mean intensities began to fall sharply, which coincided roughly with the onset of pseudocleavage (PC) furrow relaxation. Then we used this timepoint to align data across multiple embryos. We then computed means and standard errors across embryos from un-normalized data.

Measurements of PAR-3 oligomer size distribution

We measured the distribution of PAR-3 oligomer sizes during late maintenance phase in homozygous *par-1*; PAR-3::GFP mutant embryos. We first identified embryos in establishment phase before pseudocleavage. We used 30% laser power and 50 msec exposures at 1 sec intervals to focus on the cortex while minimizing photobleaching. Following pseudocleavage relaxation, we waited for 4 minutes and then acquired images in streaming mode for 50 seconds using 100% laser power and a 50 msec exposure time. For each embryo, we used hand-drawn ROIs to separate anterior and posterior features. we pooled all features detected in the first three frames and used these to estimate the distribution of PAR-3::GFP oligomer intensities. During the last 20 seconds of continuous exposure to 100% laser power, the distribution of background-subtracted feature intensities approximated a Gaussian distribution, as described previously [15]. We took the mean of a gaussian fit to this distribution as our estimate of single molecule intensities.

We used three different approaches to estimate the distribution of PAR-3 oligomer sizes. In the first approach, based on Bayesian inference, we initially assumed each feature had an equal prior probability of containing between 1 and 20 subunits. We then calculated the posterior probabilities that an observed feature contained n subunits ($0 < n <= 20$) given the conditional probabilities of an n-mer producing the observed fluorescence intensity, assuming that means and variances for the distributions of n-mer intensities were equal to the mean and variance of the single molecule distribution multiplied by n. Then we used these posterior probabilities to update the prior probabilities, repeating until the prior and posterior probability distributions converged, yielding an estimate of the steady-state size distribution. In a second approach, based on maximum likelihood estimation, we assumed that the distribution of feature intensities equals

a weighted sum of the distributions of n-mers of size 1 to 20, determining the distributions of n-mer intensities as described above. We then used the lsqnonlin function in MATLAB to compute the most likely values for each of the weights. Finally, as a third approach, we binned feature by intensity, assigning all feature with intensities in the interval [(n – 0.5)*I_sm, (n+0.5)*I_sm)] to size bin n, where I_sm is the mean intensity of single GFP molecules. Because all three approaches produced very similar results, we used the third (simplest) approach to produce the size distributions shown in Figure 3.

Measuring single molecule disappearance rates and mobilities

To measure single molecule mobilities and disappearance rates, as in Figure 5 A-C&G, and Figure S2, we imaged single PAR-3::GFP molecules in near-TIRF mode using streaming acquisition with 50 msec exposure times and 100% laser power. For some experiments, we used brief (< 5 sec) pre-exposure to 100% laser power in widefield mode to reduce the density of labeled molecules. During the first ~ 5 sec of imaging, the surface density of labeled molecules decreased rapidly to single molecule levels due to photobleaching and then decreased slowly over several minutes of observation. We collected single molecule data after the initial photobleaching interval and performed particle tracking analysis as described above. For each embryo, we used hand-drawn ROIs to separate anterior and posterior trajectories. To quantify single molecule mobilities, for all trajectories with lifetime >= 200 msec, we computed the root mean square displacements for a fixed interval (t = 200 msec). Then we plotted histograms for trajectories pooled over all embryos. To compute reference histograms for oligomers, we imaged endogenously-tagged PAR-3::GFP at the same frame rates, but with lower laser power (10%), performed tracking analysis and histogram construction as described above. To construct

reference histograms for simulated Brownian diffusion, we simulated 10,000 particles undergoing Brownian diffusion with D = 0.1 μm^2/sec, added gaussian noise with mean 0 and SD = 50 nm to approximate localization errors in our system [15], then performed tracking analysis and histogram construction as described above.

To estimate rate constants for monomer dissociation, we first estimated rate constants for disappearance of single PAR-3::GFP molecules (k_{diss}^{ant} and k_{diss}^{post}) as follows: For each embryo, we constructed release curves for anterior and posterior trajectories by plotting the number of trajectories with lifetime > t as a function of time. Plotted on a logarithmic scale, these release curves are approximately linear (i.e. they approximate exponential decay) for t > t_{min}, where t_{min} is different for anterior and posterior release curves. We used non-linear least squares (with Matlab's built-in ***fit*** function) to fit the release curves to $x(t) = x_0 e^{-k_{diss}t}$ t > t_{min}, using t_{min} = 200 msec for posterior release curves and t_{min} = 0.5 sec for anterior release curves.

To infer monomer dissociation rates k_{off} from k_{diss}^{ant} and k_{diss}^{post}, we used k_{diss}^{ant} and our measurement of k_{dep} (see below) to estimate $k_{pb} = k_{diss}^{ant} - k_{dep}$. Then, we used k_{diss}^{post} and k_{pb} to measure the monomer unbinding rate $k_{off} = k_{diss}^{post} - k_{pb}$. To estimate dissociation rates for monomeric PAR-3 (PAR-3(CR1)::GFP, we imaged single molecules of PAR-3 (PAR-3(CR1)::GFP under the same conditions used for PAR-3::GFP, measured k_{diss}^{post} as described above, and used the estimate of k_{pb} from PAR-3::GFP to infer $k_{off} = k_{diss}^{post} - k_{pb}$.

Measuring depolymerization rates

To measure depolymerization rates k_{dep}, we used a transgenic strain expressing PAR-3::GFP. We used RNAi against GFP followed by photobleaching to reduce the density of transgenic PAR-3::GFP to single molecule levels as described previously [15]. We then imaged single PAR-3 molecules using 100 % laser power and 50 msec exposures, holding photobleaching rate k_{pb} (thus total photobleaching during each exposure) constant, while varying the duty ratio of exposure (dr). For each duty ratio, we performed single particle tracking and constructed release curves as described above. We fit the release curves to exponential functions of the form $x(t) = x_0 e^{-k_{obs}t}$, using t_{min} = 1 sec to exclude the more rapid (2.7/sec) monomer dissociation. We then used MATLAB's built-in ***fit*** function to obtain a linear least squares fit to $k_{obs} = k_{dep} + dr * k_{pb}$. We took the y-intercept and slope of the linear fits as our estimates of k_{dep} and k_{pb}, respectively, and report the confidence intervals returned by the ***fit*** function.

To compare depolymerization rates in control, *par-6(RNAi);mrck-1(RNAi)* and *cdc-42(RNAi)* embryos, we imaged all embryos for 120 seconds during early maintenance phase with a 5% duty ratio, and a fixed unit exposure (50 msec at 100% laser power). We constructed release curves and measured k_{obs} for each embryo as described above using t_{min} = 2 sec. Then we used the of k_{pb} from above to estimate $k_{dep} = k_{obs} - dr * k_{pb}$ for each embryo.

Measuring oligomer size-dependent dissociation.

To measure oligomer size-dependent dissociation rates, we imaged embryos expressing NeonGreen::PAR-3 in streaming acquisition mode using 30% laser power and 50 msc exposure times during maintenance phase of embryos depleted of NMY-2. We performed particle tracking on the first 20 frames of each image sequence to avoid confounding effects of photobleaching on

oligomer size inference. We inferred the size of each tracked particle based on its initial intensity using the single molecule distribution as a standard, as described above. For each inferred oligomer size n, we computed the fraction of oligomers F_n that remained after 1 sec. Assuming a single-rate first-order dissociation reaction, we solved $F_n = e^{-k_{off}(n)}$ to estimate $k_{off}(n) = -\ln(F_n)$.

Measuring asymmetric binding of monomeric PAR-3

To measure the relative binding rates of cytoplasmic PAR-3(ΔCR1)::GFP molecules to anterior and posterior membranes, we first photobleached PAR-3(ΔCR1)::GFP molecules by exposing embryos to 100% laser power in widefield illumination mode for 5-10 seconds. We then imaged single PAR-3::GFP molecules with near-TIRF illumination using streaming acquisition with 100% laser power and 50 msec exposure times. We performed single particle tracking as described above and used hand-drawn ROIs to select anterior and posterior trajectories. We constructed the release curves as described above for trajectories with lifetimes >= 200 msec to avoid counting spurious trajectories. To estimate the total number of trajectories with lengths < 200 msec that represent membrane binding events, we used the slope of the release curve at t = 200 msec to extrapolate from t = 200 to t = 0. Finally, we used the areas of ROIs to normalize estimates of total number and used these normalized quantities to determine the ratio of anterior to posterior binding rates for each embryo.

PAR-3 depletion experiments

To obtain partial depletion of PAR-3, we placed young adult worms on RNAi feeding plates for 2-8 hours. To assess whether PAR-3 polarity was established prior to the onset of maintenance phase and whether posterior-directed cortical flows redistribute PAR-3 oligomers during maintenance phase, we imaged embryos in timelapse mode using 50 msec exposures and 30% laser power at 2.5-5 second intervals for 4 minutes following pseudocleavage relaxation. Immediately following this period, we imaged the same embryos in streaming mode with 100% laser power and 50 msec exposures for 50 seconds, and performed feature detection and oligomer size inference as described above. We determined the fluorescence density of segmented PAR-3 features in anterior and posterior ROIs and computed the anterior-posterior asymmetry of PAR-3 as the ratio of these values.

FRAP experiments

We performed FRAP experiments using the following protocol: We collected 10 images with 50 msec exposures using near-TIRF illumination at 1 second intervals using 30% laser power. We then subjected embryos to constant near-TIRF illumination with 100% laser power for 1.5 seconds to photobleach molecules at the cell surface. We then tracked recovery in timelapse mode with 50 msec exposures at 3 second intervals using 30% laser power. Because PAR-3 levels decrease during early maintenance phase, we normalized measurements of fluorescence during recovery using unbleached control data collected over the same timeframe.

References

1. Goldstein, B., and Macara, I.G. (2007). The PAR proteins: fundamental players in animal cell polarization. Dev Cell *13*, 609–622.

2. Lang, C.F., and Munro, E. (2017). The PAR proteins: from molecular circuits to dynamic self-stabilizing cell polarity. Development *144*, 3405–3416.

3. Cuenca, A.A., Schetter, A., Aceto, D., Kemphues, K., and Seydoux, G. (2003). Polarization of the C. elegans zygote proceeds via distinct establishment and maintenance phases. Development *130*, 1255–1265.

4. Cowan, C.R., and Hyman, A.A. (2004). Centrosomes direct cell polarity independently of microtubule assembly in C. elegans embryos. Nature *431*, 92–96.

5. Bienkowska, D., and Cowan, C.R. (2012). Centrosomes can initiate a polarity axis from any position within one-cell C. elegans embryos. Curr Biol *22*, 583–589.

6. Zhao, P., Teng, X., Tantirimudalige, S.N., Nishikawa, M., Wohland, T., Toyama, Y., and Motegi, F. (2019). Aurora-A Breaks Symmetry in Contractile Actomyosin Networks Independently of Its Role in Centrosome Maturation. Dev Cell *49*, 651–653. https://doi.org/10.1016/j.devcel.2019.05.010.

7. Klinkert, K., Levernier, N., Gross, P., Gentili, C., von Tobel, L., Pierron, M., Busso, C., Herrman, S., Grill, S.W., Kruse, K., et al. (2019). Aurora A depletion reveals centrosome-independent polarization mechanism in Caenorhabditis elegans. eLife *8*, e44552. https://doi.org/10.7554/eLife.44552.

8. Longhini, K.M., and Glotzer, M. (2022). Aurora A and cortical flows promote polarization and cytokinesis by inducing asymmetric ECT-2 accumulation. eLife *11*, e83992. https://doi.org/10.7554/eLife.83992.

9. Kapoor, S., and Kotak, S. (2019). Centrosome Aurora A regulates RhoGEF ECT-2 localisation and ensures a single PAR-2 polarity axis in C. elegans embryos. Development *146*, dev174565. https://doi.org/10.1242/dev.174565.

10. Cheeks, R.J., Canman, J.C., Gabriel, W.N., Meyer, N., Strome, S., and Goldstein, B. (2004). C. elegans PAR proteins function by mobilizing and stabilizing asymmetrically localized protein complexes. Curr Biol *14*, 851–862.

11. Munro, E., Nance, J., and Priess, J.R. (2004). Cortical flows powered by asymmetrical contraction transport PAR proteins to establish and maintain anterior-posterior polarity in the early C. elegans embryo. Dev Cell *7*, 413–424.

12. Motegi, F., Zonies, S., Hao, Y., Cuenca, A.A., Griffin, E., and Seydoux, G. (2011). Microtubules induce self-organization of polarized PAR domains in Caenorhabditis elegans zygotes. Nat Cell Biol *13*, 1361–1367.

13. Zonies, S., Motegi, F., Hao, Y., and Seydoux, G. (2010). Symmetry breaking and polarization of the C. elegans zygote by the polarity protein PAR-2. Development *137*, 1669–1677.

14. Goehring, N.W., Hoege, C., Grill, S.W., and Hyman, A.A. (2011). PAR proteins diffuse freely across the anterior-posterior boundary in polarized C. elegans embryos. J Cell Biol *193*, 583–594.

15. Robin, F.B., McFadden, W.M., Yao, B., and Munro, E.M. (2014). Single-molecule analysis of cell surface dynamics in Caenorhabditis elegans embryos. Nat Methods *11*, 677–682.

16. Rodriguez, J., Peglion, F., Martin, J., Hubatsch, L., Reich, J., Hirani, N., Gubieda, A.G., Roffey, J., Fernandes, A.R., St Johnston, D., et al. (2017). aPKC Cycles between Functionally Distinct PAR Protein Assemblies to Drive Cell Polarity. Dev Cell *42*, 400–415.

17. Sailer, A., Anneken, A., Li, Y., Lee, S., and Munro, E. (2015). Dynamic Opposition of Clustered Proteins Stabilizes Cortical Polarity in the C. elegans Zygote. Dev Cell *35*, 131–142.

18. Bailey, M.J., and Prehoda, K.E. (2015). Establishment of Par-Polarized Cortical Domains via Phosphoregulated Membrane Motifs. Dev Cell *35*, 199–210.

19. Hao, Y., Boyd, L., and Seydoux, G. (2006). Stabilization of cell polarity by the C. elegans RING protein PAR-2. Dev Cell *10*, 199–208.

20. Arata, Y., Hiroshima, M., Pack, C.G., Ramanujam, R., Motegi, F., Nakazato, K., Shindo, Y., Wiseman, P.W., Sawa, H., Kobayashi, T.J., et al. (2016). Cortical Polarity of the RING Protein PAR-2 Is Maintained by Exchange Rate Kinetics at the Cortical-Cytoplasmic Boundary. Cell Rep *16*, 2156–2168.

21. Hoege, C., Constantinescu, A.T., Schwager, A., Goehring, N.W., Kumar, P., and Hyman, A.A. (2010). LGL can partition the cortex of one-cell Caenorhabditis elegans embryos into two domains. Curr Biol *20*, 1296–1303.

22. Kumfer, K.T., Cook, S.J., Squirrell, J.M., Eliceiri, K.W., Peel, N., O'Connell, K.F., and White, J.G. (2010). CGEF-1 and CHIN-1 regulate CDC-42 activity during asymmetric division in the Caenorhabditis elegans embryo. Mol Biol Cell *21*, 266–277.

23. Benton, R., and St Johnston, D. (2003). Drosophila PAR-1 and 14-3-3 inhibit Bazooka/PAR-3 to establish complementary cortical domains in polarized cells. Cell *115*, 691–704.

24. Beatty, A., Morton, D.G., and Kemphues, K. (2013). PAR-2, LGL-1 and the CDC-42 GAP CHIN-1 act in distinct pathways to maintain polarity in the C. elegans embryo. Development *140*, 2005–2014.

25. Harris, T.J., and Peifer, M. (2004). Adherens junction-dependent and -independent steps in the establishment of epithelial cell polarity in Drosophila. J Cell Biol *167*, 135–147.

26. Chang, Y., and Dickinson, D.J. (2022). A particle size threshold governs diffusion and segregation of PAR-3 during cell polarization. Cell Reports *39*. https://doi.org/10.1016/j.celrep.2022.110652.

27. Oon, C.H., and Prehoda, K.E. (2019). Asymmetric recruitment and actin-dependent cortical flows drive the neuroblast polarity cycle. Elife *8*.

28. Doerflinger, H., Vogt, N., Torres, I.L., Mirouse, V., Koch, I., Nüsslein-Volhard, C., and St Johnston, D. (2010). Bazooka is required for polarisation of the Drosophila anterior-posterior axis. Development *137*, 1765–1773. https://doi.org/10.1242/dev.045807.

29. Rusan, N.M., and Peifer, M. (2007). A role for a novel centrosome cycle in asymmetric cell division. Journal of Cell Biology *177*, 13–20. https://doi.org/10.1083/jcb.200612140.

30. Rebollo, E., Sampaio, P., Januschke, J., Llamazares, S., Varmark, H., and González, C. (2007). Functionally Unequal Centrosomes Drive Spindle Orientation in Asymmetrically Dividing Drosophila Neural Stem Cells. Developmental Cell *12*, 467–474. https://doi.org/10.1016/j.devcel.2007.01.021.

31. Januschke, J., and Gonzalez, C. (2010). The interphase microtubule aster is a determinant of asymmetric division orientation in Drosophila neuroblasts. Journal of Cell Biology *188*, 693–706. https://doi.org/10.1083/jcb.200905024.

32. Shi, S.-H., Jan, L.Y., and Jan, Y.-N. (2003). Hippocampal Neuronal Polarity Specified by Spatially Localized mPar3/mPar6 and PI 3-Kinase Activity. Cell *112*, 63–75. https://doi.org/10.1016/S0092-8674(02)01249-7.

33. Inaba, M., Venkei, Z.G., and Yamashita, Y.M. (2015). The polarity protein Baz forms a platform for the centrosome orientation during asymmetric stem cell division in the Drosophila male germline. eLife *4*, e04960. https://doi.org/10.7554/eLife.04960.

34. Benton, R., and St Johnston, D. (2003). A conserved oligomerization domain in drosophila Bazooka/PAR-3 is important for apical localization and epithelial polarity. Curr Biol *13*, 1330–1334.

35. Feng, W., Wu, H., Chan, L.N., and Zhang, M. (2007). The Par-3 NTD adopts a PB1-like structure required for Par-3 oligomerization and membrane localization. EMBO J *26*, 2786–2796.

36. Zhang, Y., Wang, W., Chen, J., Zhang, K., Gao, F., Gao, B., Zhang, S., Dong, M., Besenbacher, F., Gong, W., et al. (2013). Structural insights into the intrinsic self-assembly of Par-3 N-terminal domain. Structure *21*, 997–1006.

37. Li, B., Kim, H., Beers, M., and Kemphues, K. (2010). Different domains of C. elegans PAR-3 are required at different times in development. Dev Biol *344*, 745–757.

38. McKinley, R.F., Yu, C.G., and Harris, T.J. (2012). Assembly of Bazooka polarity landmarks through a multifaceted membrane-association mechanism. J Cell Sci *125*, 1177–1190.

39. Dickinson, D.J., Schwager, F., Pintard, L., Gotta, M., and Goldstein, B. (2017). A Single-Cell Biochemistry Approach Reveals PAR Complex Dynamics during Cell Polarization. Dev Cell *42*, 416–434.

40. Illukkumbura, R., Hirani, N., Borrego-Pinto, J., Bland, T., Ng, K., Hubatsch, L., McQuade, J., Endres, R.G., and Goehring, N.W. (2023). Design principles for selective polarization of PAR proteins by cortical flows. Journal of Cell Biology *222*, e202209111. https://doi.org/10.1083/jcb.202209111.

41. Wang, S.C., Low, T.Y.F., Nishimura, Y., Gole, L., Yu, W., and Motegi, F. (2017). Cortical forces and CDC-42 control clustering of PAR proteins for Caenorhabditis elegans embryonic polarization. Nat Cell Biol *19*, 988–995.

42. Lang, C.F., and Munro, E.M. (2022). Oligomerization of peripheral membrane proteins provides tunable control of cell surface polarity. Biophysical Journal *121*, 4543–4559. https://doi.org/10.1016/j.bpj.2022.10.035.

43. Joberty, G., Petersen, C., Gao, L., and Macara, I.G. (2000). The cell-polarity protein Par6 links Par3 and atypical protein kinase C to Cdc42. Nat Cell Biol *2*, 531–539. https://doi.org/10.1038/35019573.

44. Lin, D., Edwards, A.S., Fawcett, J.P., Mbamalu, G., Scott, J.D., and Pawson, T. (2000). A mammalian PAR-3–PAR-6 complex implicated in Cdc42/Rac1 and aPKC signalling and cell polarity. Nat Cell Biol *2*, 540–547. https://doi.org/10.1038/35019582.

45. Qiu, R.-G., Abo, A., and Martin, G.S. (2000). A human homolog of the *C. elegans* polarity determinant Par-6 links Rac and Cdc42 to PKCζ signaling and cell transformation. Current Biology *10*, 697–707. https://doi.org/10.1016/S0960-9822(00)00535-2.

46. Noda, Y., Takeya, R., Ohno, S., Naito, S., Ito, T., and Sumimoto, H. (2001). Human homologues of the Caenorhabditis elegans cell polarity protein PAR6 as an adaptor that links the small GTPases Rac and Cdc42 to atypical protein kinase C. Genes to Cells *6*, 107–119. https://doi.org/10.1046/j.1365-2443.2001.00404.x.

47. Garrard, S.M., Capaldo, C.T., Gao, L., Rosen, M.K., Macara, I.G., and Tomchick, D.R. (2003). Structure of Cdc42 in a complex with the GTPase-binding domain of the cell polarity protein, Par6. The EMBO Journal *22*, 1125–1133. https://doi.org/10.1093/emboj/cdg110.

48. Li, J., Kim, H., Aceto, D.G., Hung, J., Aono, S., and Kemphues, K.J. (2010). Binding to PKC-3, but not to PAR-3 or to a conventional PDZ domain ligand, is required for PAR-6 function in C. elegans. Dev Biol *340*, 88–98.

49. Renschler, F.A., Bruekner, S.R., Salomon, P.L., Mukherjee, A., Kullmann, L., Schütz-Stoffregen, M.C., Henzler, C., Pawson, T., Krahn, M.P., and Wiesner, S. (2018). Structural basis for the interaction between the cell polarity proteins Par3 and Par6. Science Signaling *11*, eaam9899. https://doi.org/10.1126/scisignal.aam9899.

50. Holly, R.W., Jones, K., and Prehoda, K.E. (2020). A Conserved PDZ-Binding Motif in aPKC Interacts with Par-3 and Mediates Cortical Polarity. Current Biology *30*, 893-898.e5. https://doi.org/10.1016/j.cub.2019.12.055.

51. Beers, M., and Kemphues, K. (2006). Depletion of the co-chaperone CDC-37 reveals two modes of PAR-6 cortical association in C. elegans embryos. Development *133*, 3745–3754.

52. Deutz, L.N., Sarıkaya, S., and Dickinson, D.J. (2023). Membrane extraction in native lipid nanodiscs reveals dynamic regulation of Cdc42 complexes during cell polarization. Biophysical Journal. https://doi.org/10.1016/j.bpj.2023.11.021.

53. Watts, J.L., Etemad-Moghadam, B., Guo, S., Boyd, L., Draper, B.W., Mello, C.C., Priess, J.R., and Kemphues, K.J. (1996). par-6, a gene involved in the establishment of asymmetry in early C. elegans embryos, mediates the asymmetric localization of PAR-3. Development *122*, 3133–3140.

54. Ramanujam, R., Han, Z., Zhang, Z., Kanchanawong, P., and Motegi, F. (2018). Establishment of the PAR-1 cortical gradient by the aPKC-PRBH circuit. Nat Chem Biol *14*, 917–927. https://doi.org/10.1038/s41589-018-0117-1.

55. Goehring, N.W., Trong, P.K., Bois, J.S., Chowdhury, D., Nicola, E.M., Hyman, A.A., and Grill, S.W. (2011). Polarization of PAR proteins by advective triggering of a pattern-forming system. Science *334*, 1137–1141.

56. Fletcher, G.C., Lucas, E.P., Brain, R., Tournier, A., and Thompson, B.J. (2012). Positive feedback and mutual antagonism combine to polarize Crumbs in the Drosophila follicle cell epithelium. Curr Biol *22*, 1116–1122. https://doi.org/10.1016/j.cub.2012.04.020.

57. Wang, Y.C., Khan, Z., Kaschube, M., and Wieschaus, E.F. (2012). Differential positioning of adherens junctions is associated with initiation of epithelial folding. Nature *484*, 390–393.

58. Simões, S. de M., Blankenship, J.T., Weitz, O., Farrell, D.L., Tamada, M., Fernandez-Gonzalez, R., and Zallen, J.A. (2010). Rho-Kinase Directs Bazooka/Par-3 Planar Polarity

during *Drosophila* Axis Elongation. Developmental Cell *19*, 377–388. https://doi.org/10.1016/j.devcel.2010.08.011.

59. Bland, T., Hirani, N., Briggs, D.C., Rossetto, R., Ng, K., Taylor, I.A., McDonald, N.Q., Zwicker, D., and Goehring, N.W. (2024). Optimized PAR-2 RING dimerization mediates cooperative and selective membrane binding for robust cell polarity. The EMBO Journal *43*, 3214–3239. https://doi.org/10.1038/s44318-024-00123-3.

60. Dodgson, J., Chessel, A., Yamamoto, M., Vaggi, F., Cox, S., Rosten, E., Albrecht, D., Geymonat, M., Csikasz-Nagy, A., Sato, M., et al. (2013). Spatial segregation of polarity factors into distinct cortical clusters is required for cell polarity control. Nat Commun *4*, 1834.

61. Rincon, S.A., Bhatia, P., Bicho, C., Guzman-Vendrell, M., Fraisier, V., Borek, W.E., Alves, F. d. e. L., Dingli, F., Loew, D., Rappsilber, J., et al. (2014). Pom1 regulates the assembly of Cdr2-Mid1 cortical nodes for robust spatial control of cytokinesis. J Cell Biol *206*, 61–77.

62. Budnar, S., Husain, K.B., Gomez, G.A., Naghibosadat, M., Varma, A., Verma, S., Hamilton, N.A., Morris, R.G., and Yap, A.S. (2019). Anillin Promotes Cell Contractility by Cyclic Resetting of RhoA Residence Kinetics. Developmental Cell *49*, 894-906.e12. https://doi.org/10.1016/j.devcel.2019.04.031.

63. Vargas, E., and Prehoda, K.E. (2023). Negative cooperativity underlies dynamic assembly of the Par complex regulators Cdc42 and Par-3. Journal of Biological Chemistry *299*, 102749. https://doi.org/10.1016/j.jbc.2022.102749.

64. Packer, J., Gubieda, A.G., Brooks, A., Deutz, L.N., Squires, I., Ellison, S., Schneider, C., Naganathan, S.R., Wollman, A.J.M., Dickinson, D.J., et al. (2024). Atypical Protein Kinase C Promotes its own Asymmetric Localisation by Phosphorylating Cdc42 in the C. elegans zygote. Preprint at bioRxiv, https://doi.org/10.1101/2023.10.27.563985 https://doi.org/10.1101/2023.10.27.563985.

65. Holly, R.W., and Prehoda, K.E. (2019). Phosphorylation of Par-3 by Atypical Protein Kinase C and Competition between Its Substrates. Developmental Cell *49*, 678–679. https://doi.org/10.1016/j.devcel.2019.05.002.

66. Soriano, E.V., Ivanova, M.E., Fletcher, G., Riou, P., Knowles, P.P., Barnouin, K., Purkiss, A., Kostelecky, B., Saiu, P., Linch, M., et al. (2016). aPKC Inhibition by Par3 CR3 Flanking Regions Controls Substrate Access and Underpins Apical-Junctional Polarization. Developmental Cell *38*, 384–398. https://doi.org/10.1016/j.devcel.2016.07.018.

67. Munro, E. (2017). Protein Clustering Shapes Polarity Protein Gradients. Dev Cell *42*, 309–311.

68. Duncan, F.E., Moss, S.B., Schultz, R.M., and Williams, C.J. (2005). PAR-3 defines a central subdomain of the cortical actin cap in mouse eggs. Dev Biol *280*, 38–47. https://doi.org/10.1016/j.ydbio.2004.12.034.

69. Brenner, S. (1974). The genetics of Caenorhabditis elegans. Genetics *77*, 71–94.

70. Timmons, L., Court, D.L., and Fire, A. (2001). Ingestion of bacterially expressed dsRNAs can produce specific and potent genetic interference in Caenorhabditis elegans. Gene *263*, 103–112.

71. Kamath, R.S., Fraser, A.G., Dong, Y., Poulin, G., Durbin, R., Gotta, M., Kanapin, A., Le Bot, N., Moreno, S., Sohrmann, M., et al. (2003). Systematic functional analysis of the Caenorhabditis elegans genome using RNAi. Nature *421*, 231–237. https://doi.org/10.1038/nature01278.

72. Crocker, J.C., and Grier, D.G. (1996). Methods of Digital Video Microscopy for Colloidal Studies. Journal of Colloid and Interface Science *179*, 298–310. https://doi.org/10.1006/jcis.1996.0217.

73. Jaqaman, K., Loerke, D., Mettlen, M., Kuwata, H., Grinstein, S., Schmid, S.L., and Danuser, G. (2008). Robust single-particle tracking in live-cell time-lapse sequences. Nat Methods *5*, 695–702. https://doi.org/10.1038/nmeth.1237.

Figure 1

Lang et al, Figure 1

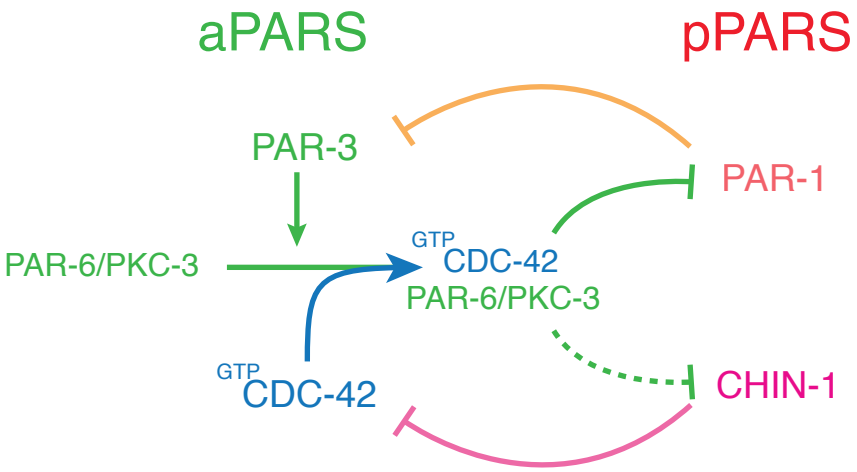

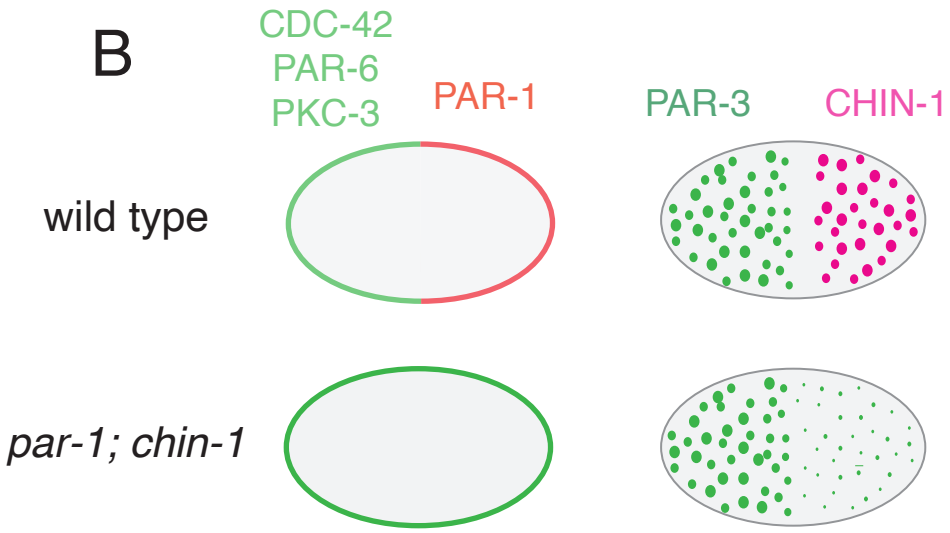

Figure 2

Lang et al, Figure 2

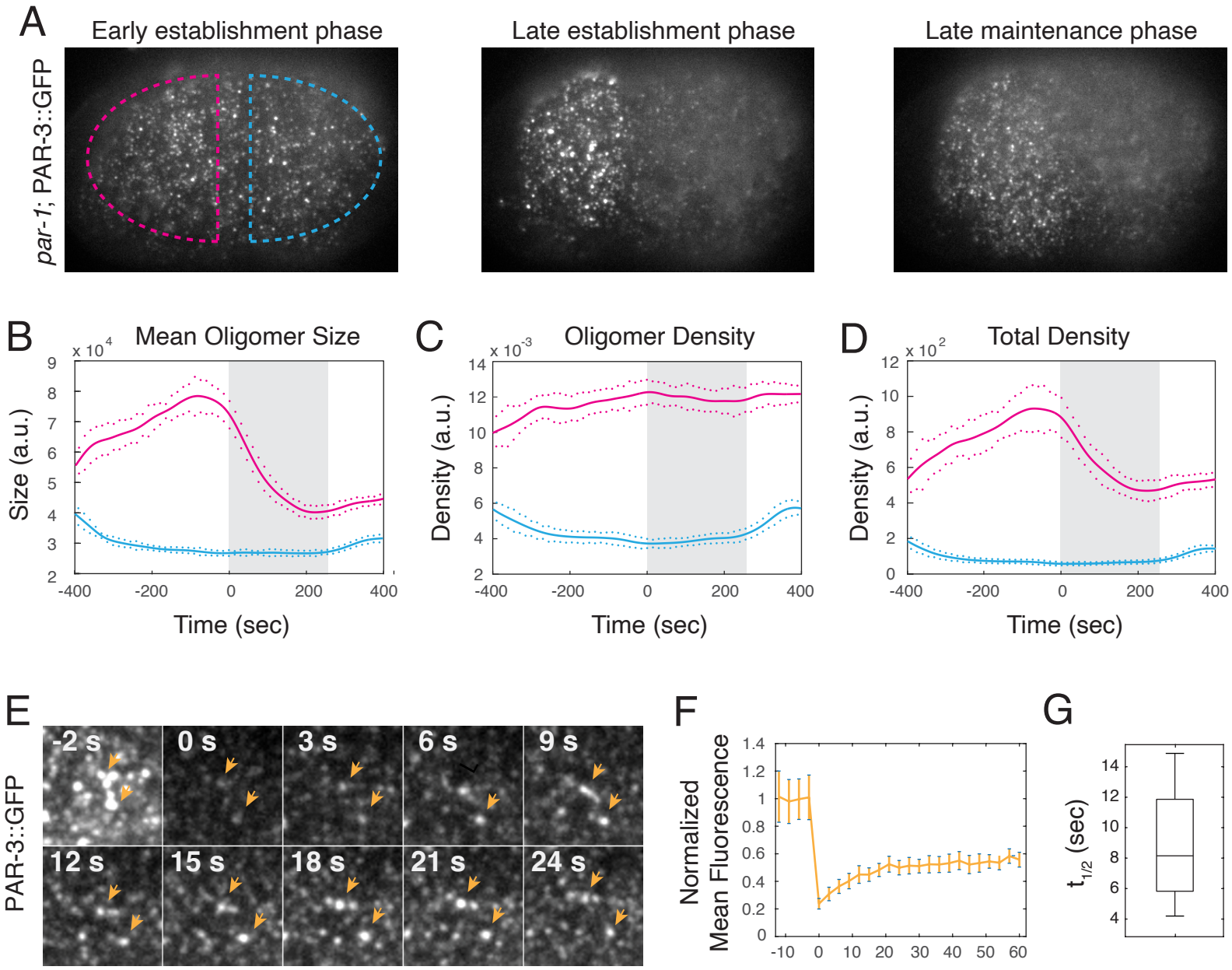

Figure 3

Lang et al, Figure 3

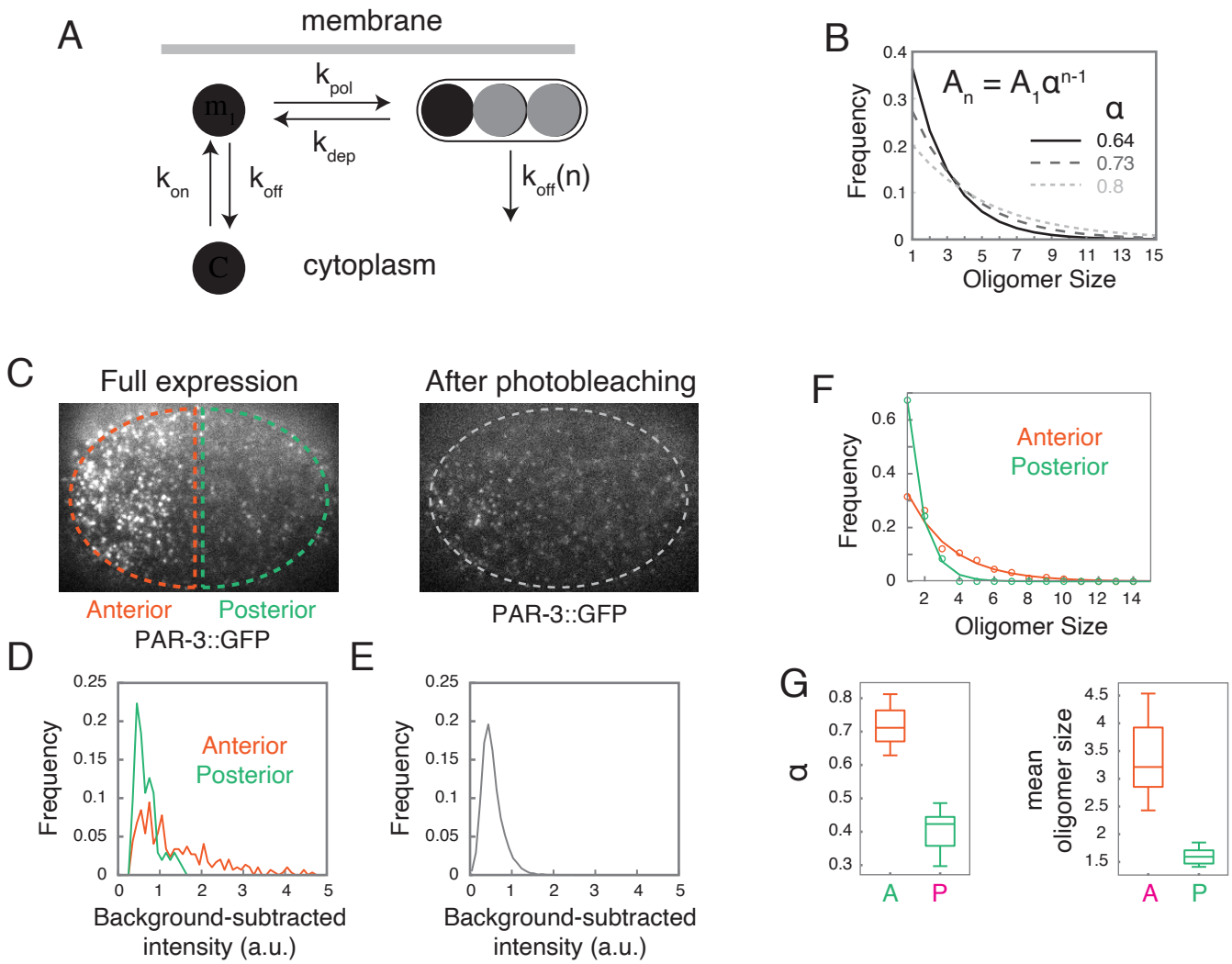

Figure 4

Lang et al, Figure 4

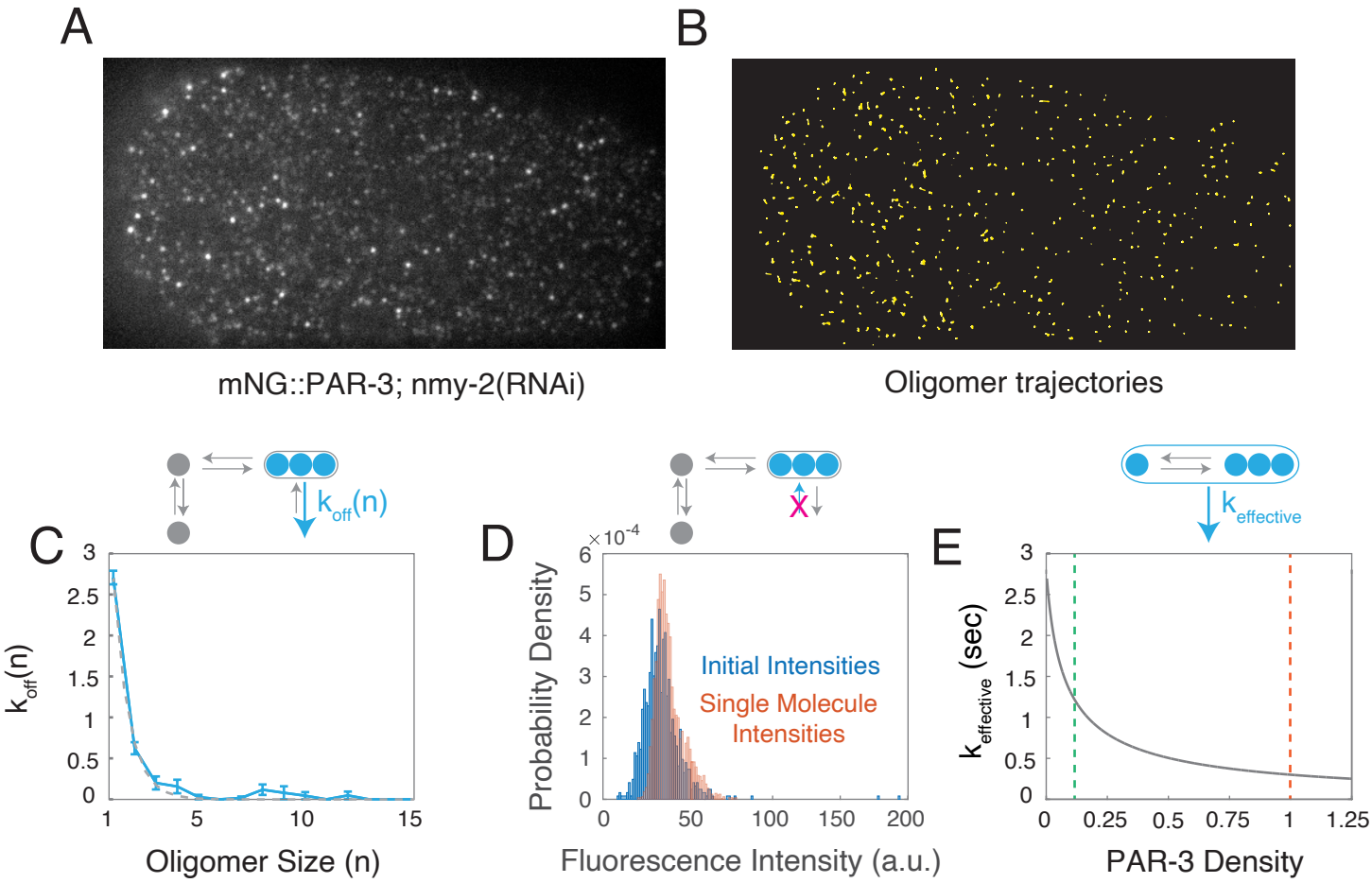

Figure 5

Lang et al, Figure 5

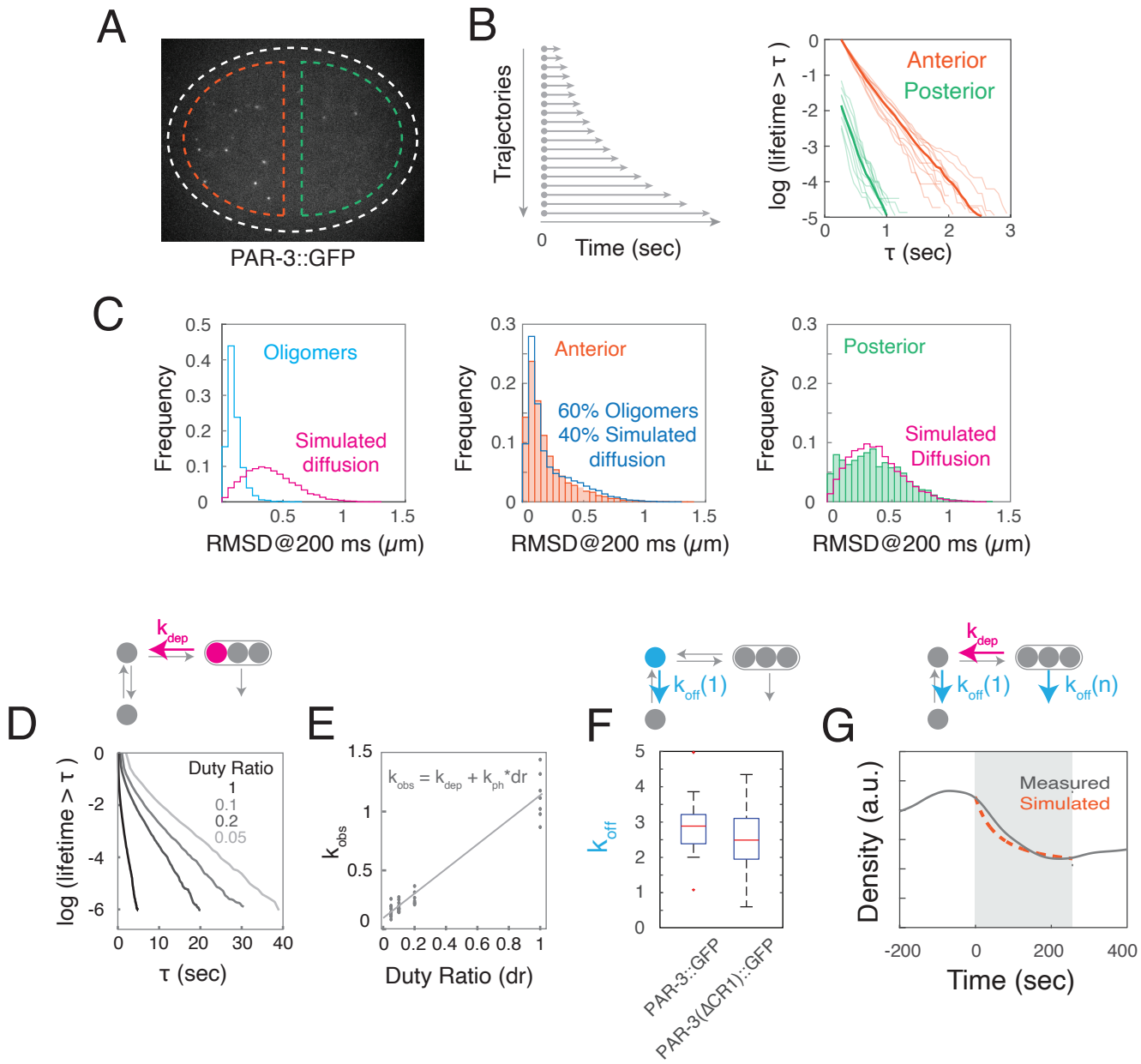

Figure 6

Lang et al, Figure 6

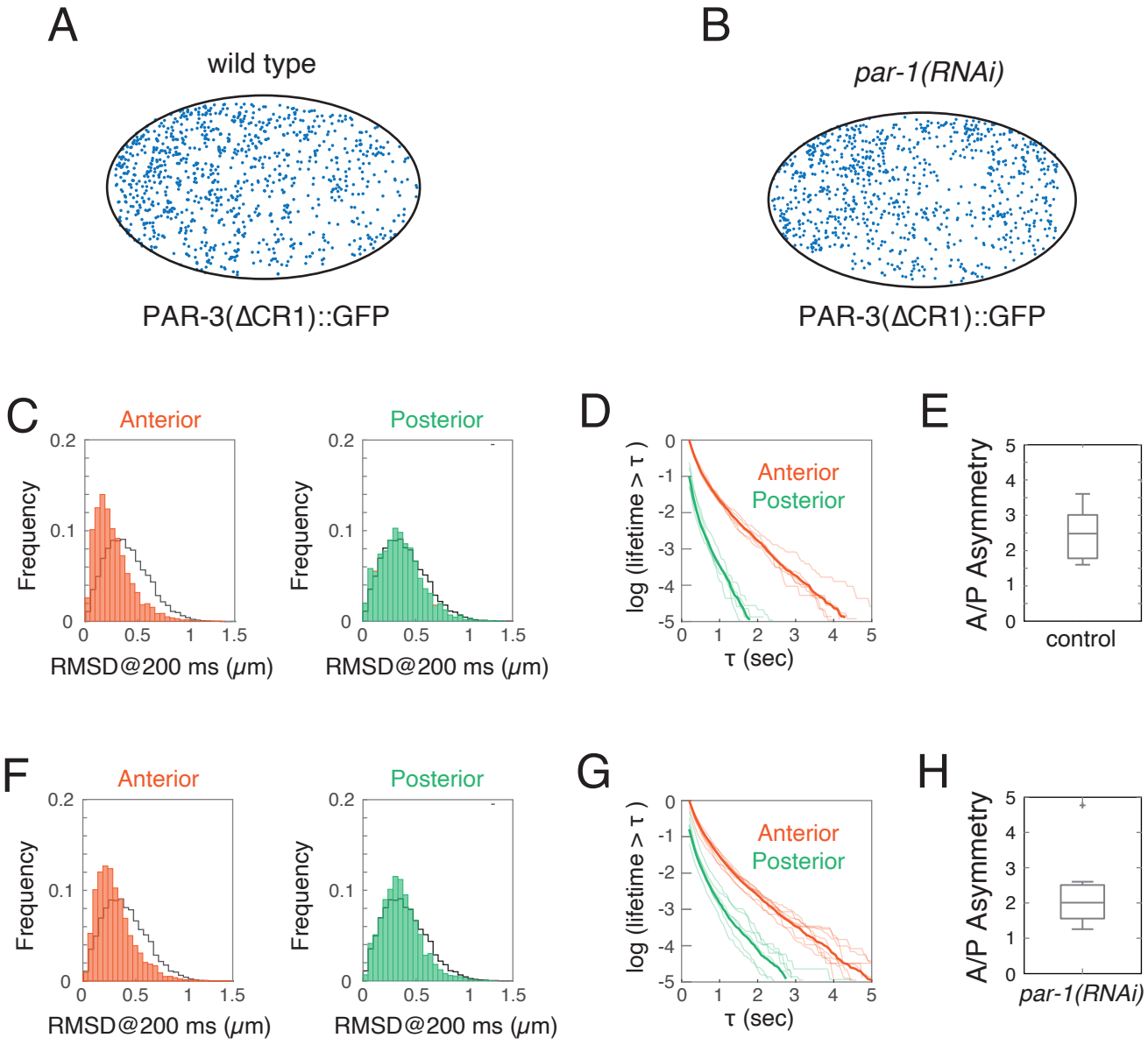

Figure 7

Lang et al, Figure 7

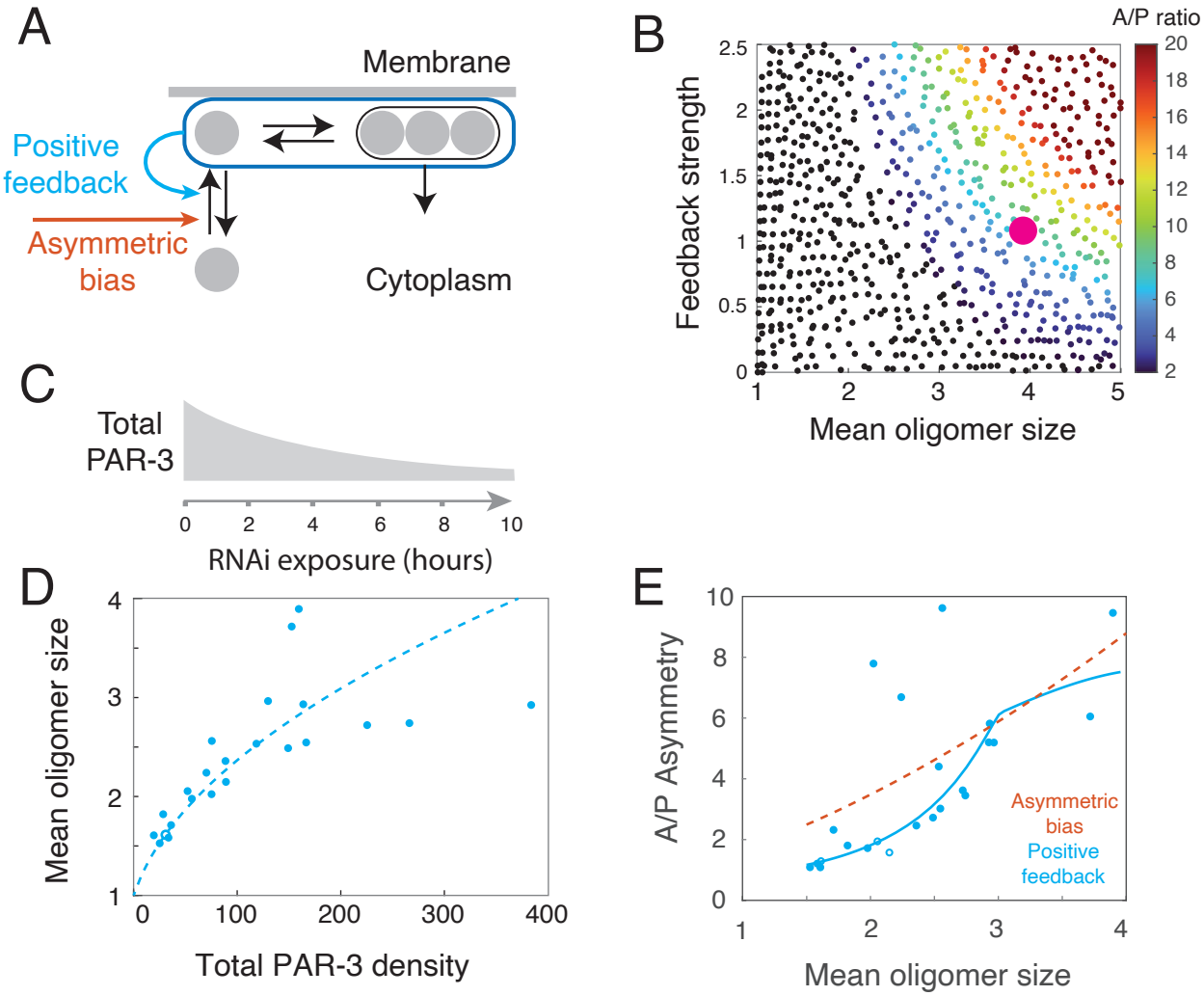

Figure 8

Lang et al, Figure 8

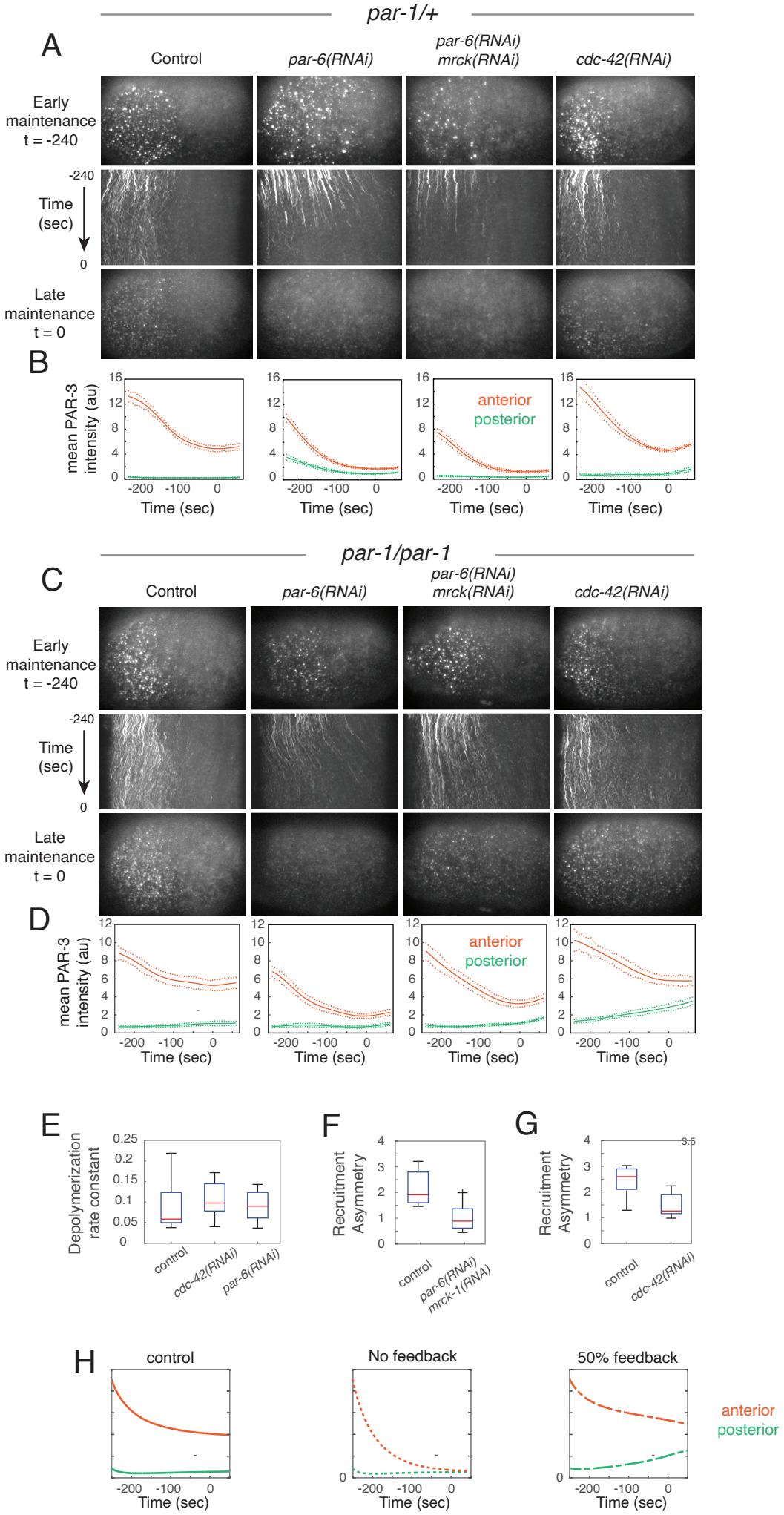

Figure S1

Lang et al, Figure S1

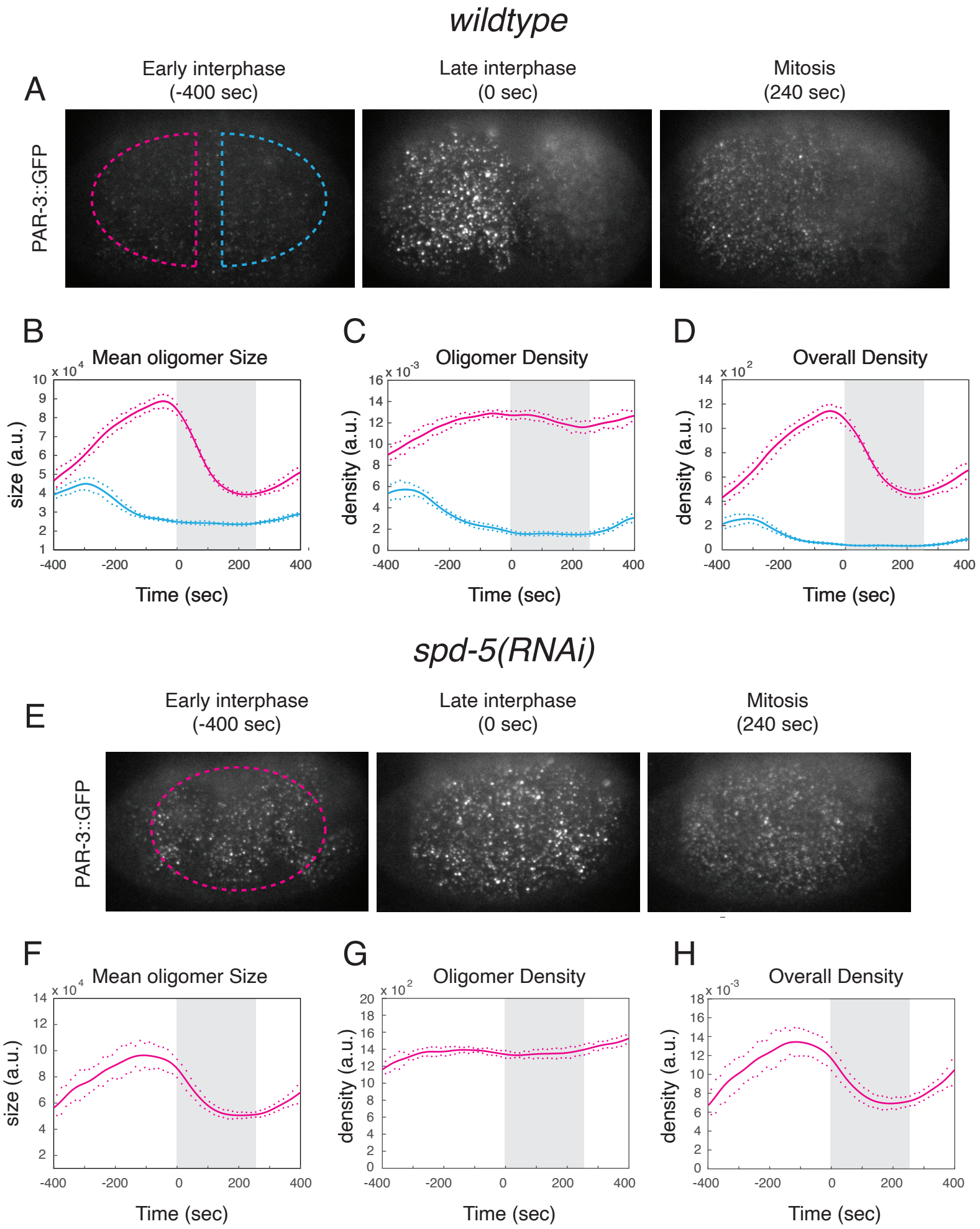

Figure S2

Lang et al, Figure S2

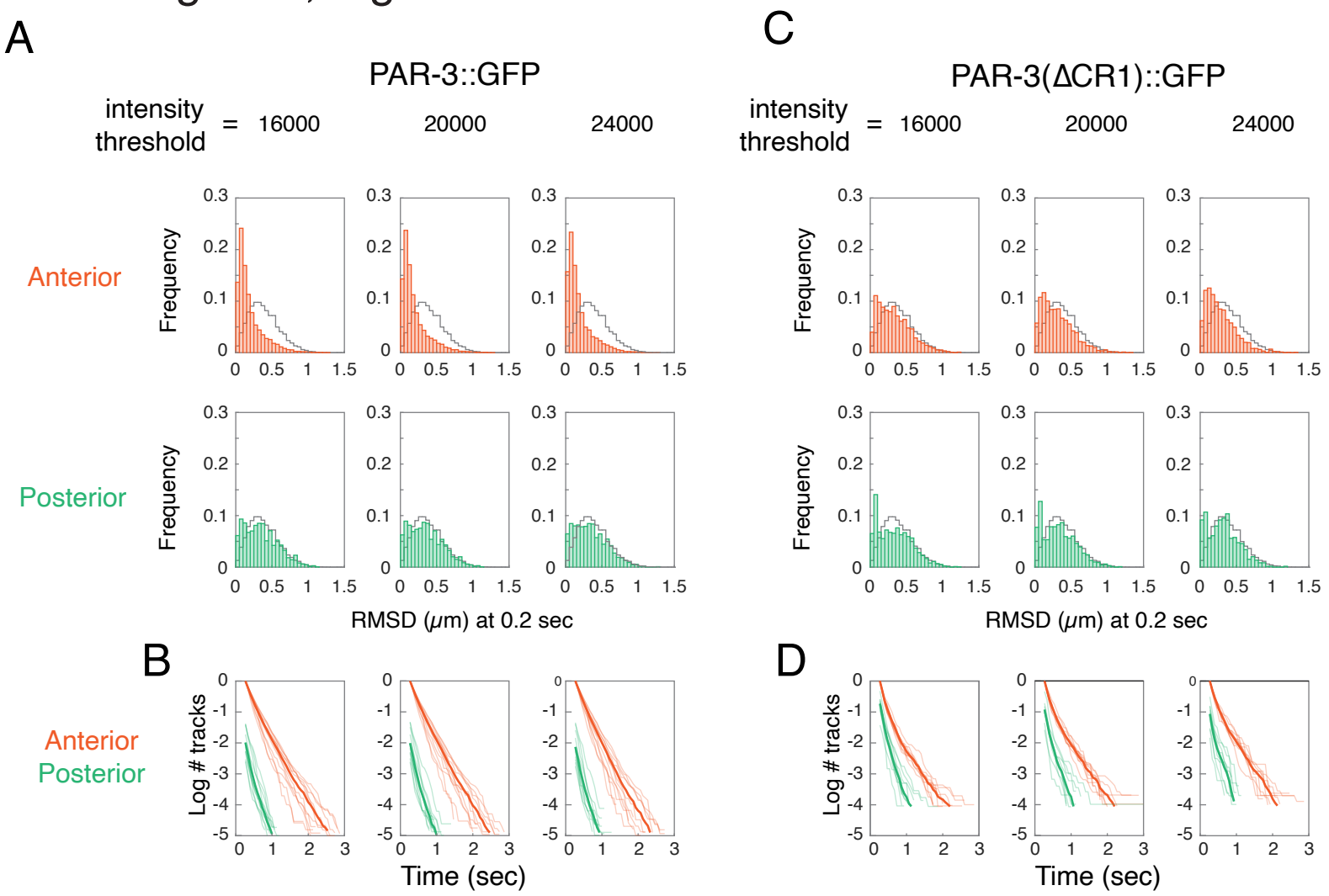

Figure S3

Lang et al, Figure S3

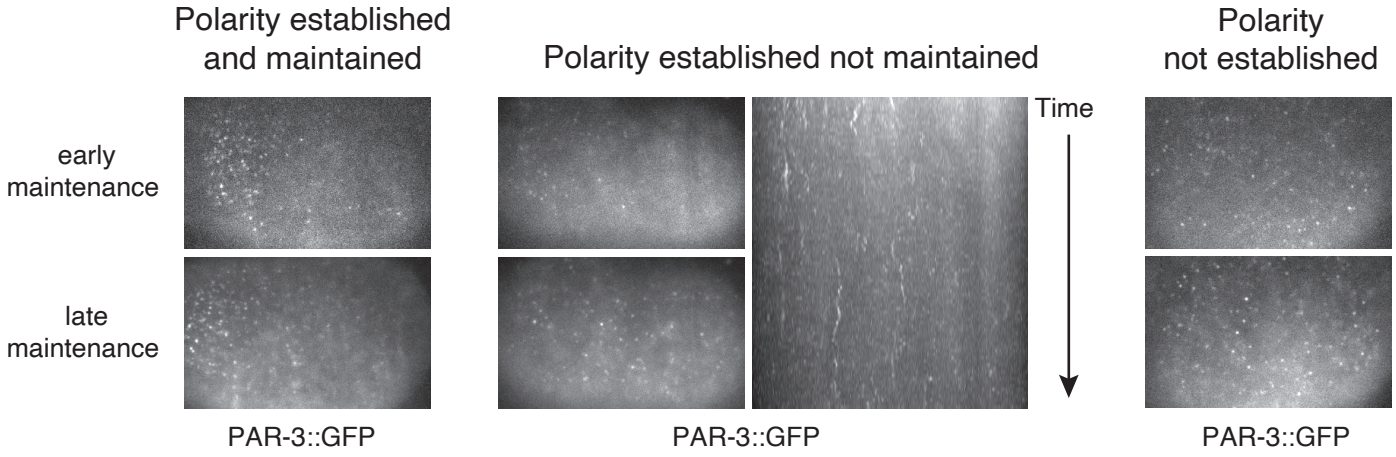

Figure S4

Lang et al, Figure S4

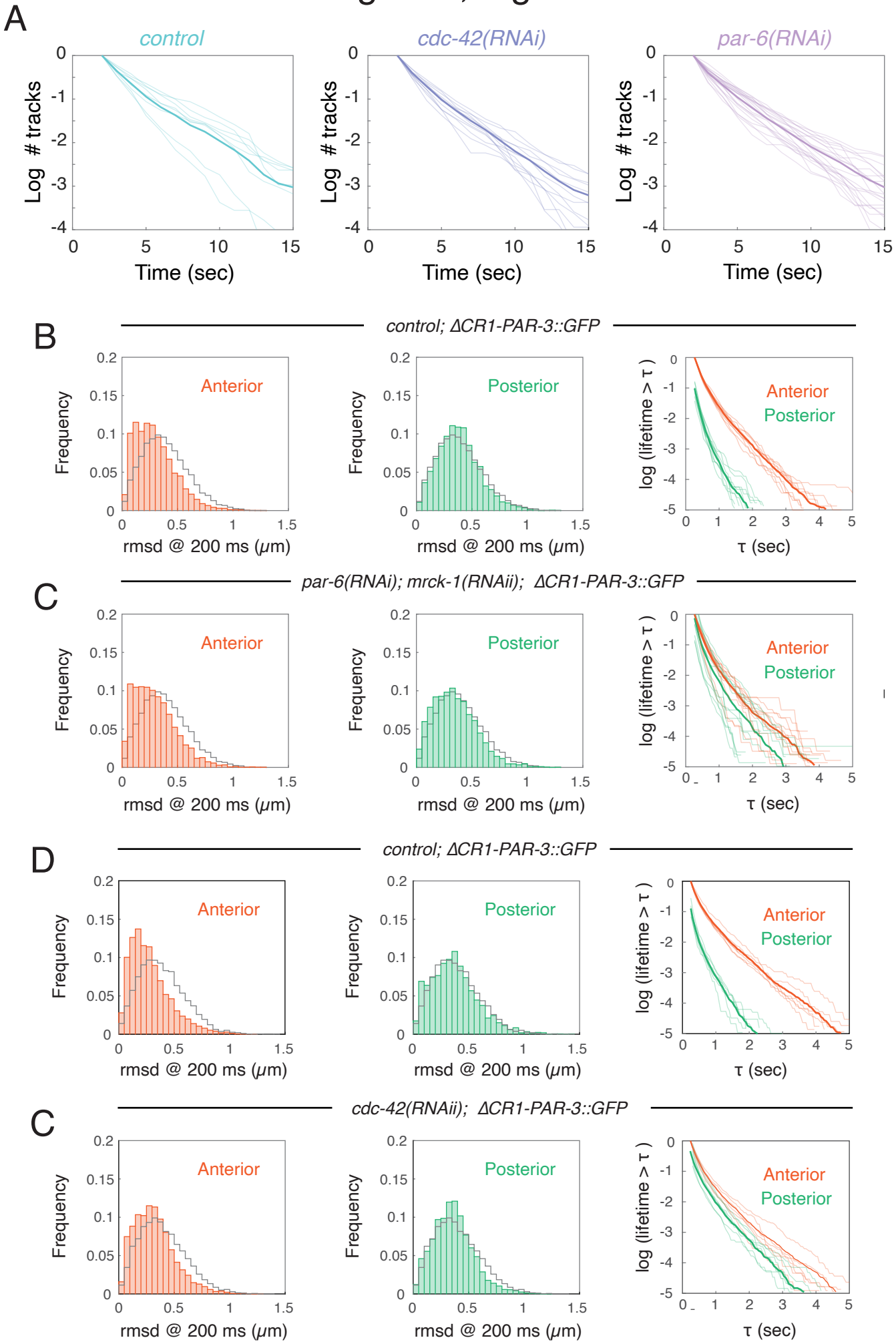

Figure S5

Lang et al, Figure S5

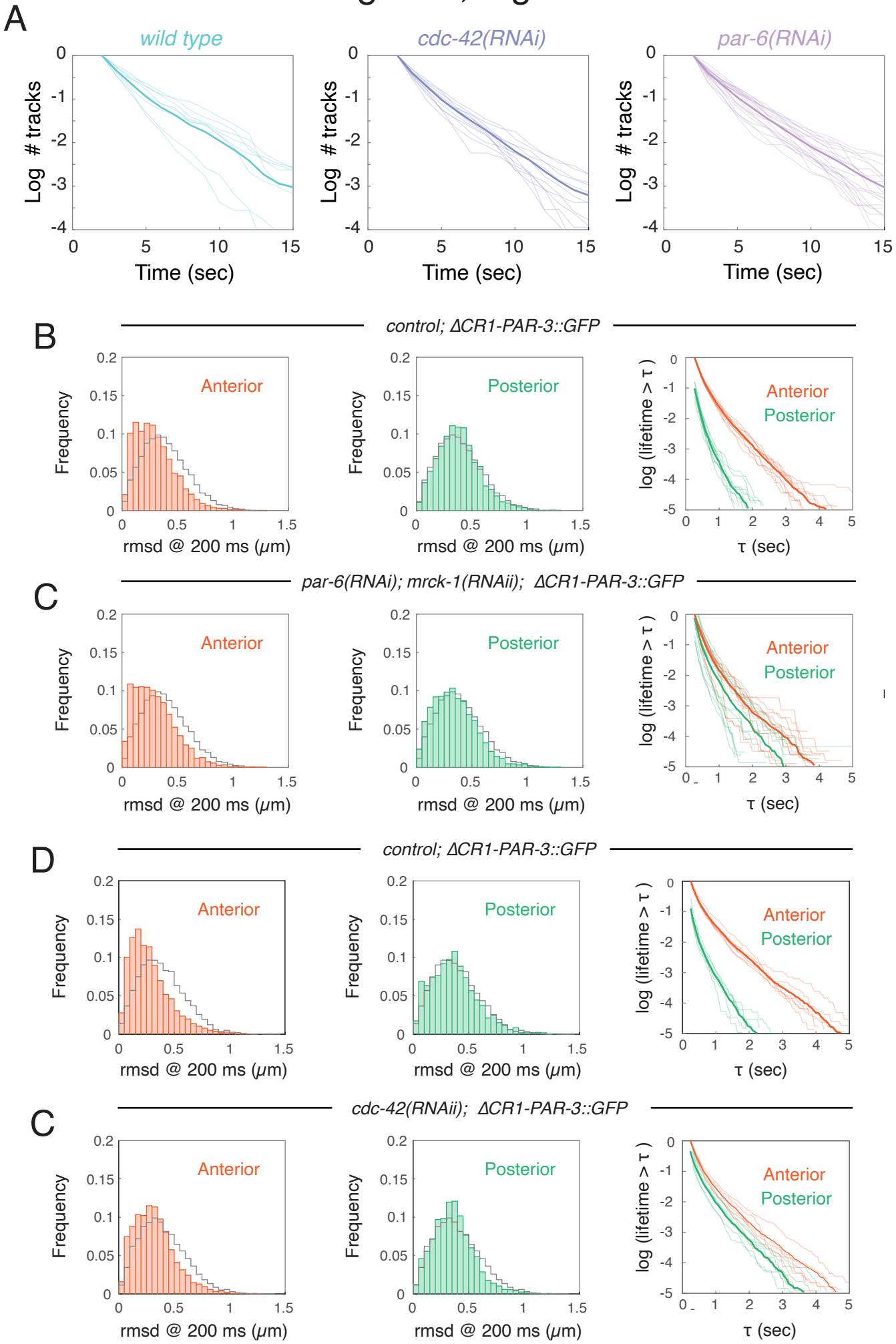

Mathematical appendix: Oligomerization and positive feedback on membrane recruitment encode dynamically stable PAR-3 asymmetries in the C. elegans zygote

Charles F. Lang, Ondrej Maxian, Alexander Anneken, and Edwin M. Munro

In this section we describe the derivation, parameterization and analysis of a mathematical model for PAR-3 kinetics. The basic approach follows our previous theoretical analysis of oligomerization by peripheral membrane binding proteins [6]. Briefly, as schematized in Figs. 3A and 7A, we assume a well-mixed cytoplasmic pool of PAR-3 monomers which bind reversibly to the plasma membrane. At the membrane, monomers assemble reversibly into linear oligomers with size-dependent mobilities and dissociation rates. Finally, we assume that membrane-bound PAR-3 feeds back indirectly to promote the attachment of PAR-3 monomers to the membrane. Letting $A_n(x)$ be the density (number/length) of membrane-bound oligomers of size n at point x, and A_{c} be the concentration of cytoplasmic PAR-3, the density of membrane-bound oligomers evolves according to the following equations [6, Eq. (1)]

$$\partial_t A_1 = D_1 \partial_x^2 A_1 + (k_{\mathrm{basal}} + k_f f(A))\, A_{\mathrm{c}} - k_{\mathrm{off}} A_1 \tag{M1a}$$

$$+ 2k_{\mathrm{dep}} A_2 - 2k_{\mathrm{pol}} A_1^2 + \sum_{n=3}^{N} (k_{\mathrm{dep}} A_n - k_{\mathrm{pol}} A_1 A_{n-1})$$

$$\partial_t A_n = k_{\mathrm{pol}} A_1 (A_{n-1} - A_n) - k_{\mathrm{dep}} (A_n - A_{n+1}) \qquad N > n \geq 2 \tag{M1b}$$

$$\partial_t A_N = k_{\mathrm{pol}} A_1 A_{N-1} - k_{\mathrm{dep}} A_N \tag{M1c}$$

$$A_{\mathrm{c}} = \frac{1}{hL}\left(A^{(\mathrm{Tot})} L - \int_0^L A(x)\, dx\right) \qquad A(x) = \sum_{n=1}^{N} n A_n(x). \tag{M1d}$$

The first line of (M1a) describes the membrane attachment and detachment of PAR-3 monomers, with basal rates governed by k_{basal} and k_{off}, and density-dependent feedback on monomer attachment governed by $k_f f(A)$, whose form we consider below. The second line of (M1a), combined

with (M1b) and (M1c), describes the dynamics of polymerization on the membrane, with forward and reverse rate constants k_{pol} and k_{dep}. Finally, the cytoplasmic concentration A_{c} is determined in (M1d) from the conservation of total protein in the system, where $A(x)$ is the total bound density at each point on the membrane and $A^{(\text{Tot})}$ is the density when all PAR-3 is uniformly bound to the membrane.

The forms of equations (M1) reflect several important simplifying assumptions, which are justified by our experimental observations. First, our experimental data (Fig. 3K) show that oligomer mobilities and dissociation rates fall sharply with increasing oligomer size. Therefore we neglect both oligomer diffusion and detachment, as in [6]. Second, our experimental observations (see main text) suggest that direct attachment of cytoplasmic monomers to membrane-bound PAR-3 oligomers makes a relatively small contribution to the total flux of PAR-3 monomers onto the membrane. In previous work [6], we showed that direct attachment effectively reduces or increases the strength of indirect feedback, depending on the regime considered. Thus we do not explicitly model the direct attachment of cytoplasmic monomers to membrane-bound oligomers, instead assuming that the weak effects of this attachment are implicit in the feedback strength.

1 Nondimensionalization and parameter estimation

To estimate the model parameters and compare model predictions to experimental observations, we scale the equations by appropriate density ($A^{(\text{Tot,WT})}$, which represents $A^{(\text{Tot})}$ under wild type conditions), length (L), and time ($1/k_{\text{dep}}$) scales. Since polymerization dynamics are much slower than detachment, ($1/k_{\text{dep}}$) is the time a typical PAR-3 molecule spends on the membrane. Accordingly, we define the dimensionless (hatted) variables

$$x = \hat{x}L, \qquad t = \hat{t}/k_{\text{dep}}, \qquad A = \hat{A}A^{(\text{Tot,WT})}.$$

Substituting into (M1) gives dynamics in non-dimensional form [6, Eq. 14]

$$\partial_{\hat{t}}\hat{A}_1 = \hat{D}_1\partial_{\hat{x}}^2\hat{A}_1 + \hat{K}_{\rm on}\left(1+\hat{K}_{\rm f}\hat{F}(\hat{A})\right)\hat{A}_{\rm c} - \hat{K}_{\rm off}\hat{A}_1$$
$$+ 2\hat{A}_2 - 2\hat{K}_{\rm p}\hat{A}_1{}^2 + \sum_{n=3}^{N}\left(\hat{A}_n - \hat{K}_{\rm p}\hat{A}_1\hat{A}_{n-1}\right) \tag{M2a}$$

$$\partial_{\hat{t}}\hat{A}_n = \hat{K}_{\rm p}\hat{A}_1(\hat{A}_{n-1}-\hat{A}_n) - (\hat{A}_n - \hat{A}_{n+1}) \qquad N > n \geq 2 \tag{M2b}$$

$$\partial_t\hat{A}_N = \hat{K}_{\rm p}\hat{A}_1\hat{A}_{N-1} - \hat{A}_N \tag{M2c}$$

$$\hat{A}_{\rm c} = \hat{A}^{(\rm Tot)} - \int_0^1 \hat{A}(x)\,d\hat{x}, \tag{M2d}$$

Equations (M2) involve six dimensionless parameters

$$\hat{D}_1 = \frac{D_1}{L^2 k_{\rm dep}}, \quad \hat{K}_{\rm on} = \frac{k_{\rm basal}}{k_{\rm dep}h}, \quad \hat{K}_{\rm f} = \frac{k_f A^{(\rm Tot,WT)}}{k_{\rm basal}}, \tag{M2e}$$
$$\hat{K}_{\rm off} = \frac{k_{\rm off}}{k_{\rm dep}}, \quad \hat{K}_{\rm p} = \frac{k_{\rm pol}A^{(\rm Tot,WT)}}{k_{\rm dep}}, \quad \hat{A}^{(\rm Tot)} = \frac{A^{(\rm Tot)}}{A^{(\rm Tot,WT)}}, \quad \hat{F}(\hat{A}) = \frac{f(A)}{A^{(\rm Tot,WT)}}.$$

(and the feedback function $F(\hat{A})$; see below), whose values we determine by direct measurement or by fitting to experimental data. Our data directly give values for three dimensional parameters: the monomeric diffusion coefficient $D_1 = 0.1\ \mu\text{m}^2/\text{s}$, the monomer detachment rate $k_{\rm off} = 3/\text{s}$, and the rate at which single subunits unbind from PAR-3 oligomers (0.08/s), which gives $k_{\rm dep} = 0.16/\text{s}$ (since unbinding can occur from either side). We take the length scale $L = 134.6\ \mu\text{m}$ to be the perimeter length of the maximal cross-section of an ellipsoid, with half-axis lengths $27 \times 15 \times 15$ μm, which approximates the shape and dimensions of a typical *C. elegans* embryo in mitosis [2]. Together, these measurements determine values for the non-dimensional parameters $\hat{D}_1$ and $\hat{K}_{\rm off}$. The parameter $\hat{A}^{(\rm Tot)}$ represents a depletion factor; it is 1 in wild-type embryos and later varied to mimic depletion of PAR-3.

1.1 Oligomerization and effective dissociation

To fit the polymerization rate $\hat{K}_{\rm p}$, we first solve (M2) at steady state to obtain an exponential distribution of oligomer sizes [1, 6]

$$\hat{A}_n = \hat{K}_{\rm p}\hat{A}_1\hat{A}_{n-1} := \alpha\hat{A}_{n-1} \quad n \geq 2. \tag{M3}$$

This defines $\alpha = \hat{K}_{\rm p}\hat{A}_1 = (k_{\rm pol}/k_{\rm dep})\,A_1$ as the coefficient of the exponential distribution of oligomer sizes. It follows that the total amount of PAR-3 is given by

$$\hat{A} = \sum_{n=1}^{N} n\alpha^{n-1}\hat{A}_1 \xrightarrow{N\to\infty} \frac{\hat{A}_1}{(1-\alpha)^2}. \tag{M4}$$

This equation can then be solved for $\hat{A}_1$ to obtain [6, Eq. (12)]

$$\hat{A}_1 = \frac{1 + 2\hat{A}\hat{K}_\mathrm{p} - \sqrt{1 + 4\hat{K}_\mathrm{p}\hat{A}}}{2\hat{A}\left(\hat{K}_\mathrm{p}\right)^2}, \tag{M5}$$

which gives the number of bound monomers (and therefore α) as a function[1] of the total bound $\hat{A}$. To fit the value of $\hat{K}_\mathrm{p}$, we use our measurements from the polarized state in *par-1* mutant embryos (Fig. 3). Our particular assumption is that there is roughly 25% bound PAR-3 during maintenance phase,[2] which gives $\hat{A} \approx 0.4$ on the anterior. Combining this with our measurement $\alpha = 0.73$ on the anterior cortex (Fig. 3H), we choose $\hat{K}_\mathrm{p}$ such that $\alpha\left(\hat{K}_\mathrm{p}, \hat{A} = 0.4\right) = 0.73$, which gives an estimate $\hat{K}_\mathrm{p} = 25$. The corresponding value of α on the posterior (where $\hat{A} = 0.4/8 = 0.05$) is predicted to be $\alpha\left(\hat{K}_\mathrm{p} = 25, \hat{A} = 0.05\right) = 0.42$, in precise agreement with experimental observations.

Once $\hat{K}_\mathrm{p}$ is known, we can compute the effective dissociation rate (Fig. 4E) by assuming that the distribution of oligomer sizes is given by (M3), with detachment rates given by $k_\mathrm{off}^{(n)} = k_\mathrm{off}^{(1)}\beta^{n-1}$. This gives the effective dissociation rate

$$k_\mathrm{effective} = \frac{k_\mathrm{off}^{(1)}\hat{A}_1}{\hat{A}}\sum_{n=1}^{\infty} n\alpha^{n-1}\beta^{n-1} = \frac{k_\mathrm{off}^{(1)}\hat{A}_1}{\hat{A}\left(1-\alpha\beta\right)^2} = k_\mathrm{off}^{(1)}\left(\frac{1-\alpha}{1-\alpha\beta}\right)^2, \tag{M6}$$

where $\alpha(\hat{A}) = \hat{A}_1(\hat{A})\hat{K}_\mathrm{p}$ is obtained using (M3) again. This results is shown in Fig. 4E; note however that using an exponential relationship for the oligomer sizes and a nonzero detachment rate for oligomer sizes larger than one is inconsistent at steady state.

1.2 The form of the feedback strength and resulting steady states

To fit the remaining dimensionless parameters[3] $\hat{K}_\mathrm{on}$ and $\hat{K}_\mathrm{f}$, we seek values for which model predictions match steady state behaviors observed in wild type and *spd-5(RNAi)* embryos. First, because PAR-3 distributions remain roughly uniform throughout polarity establishment and maintenance

[1] This convenient closed-form expression is a consequence of our neglect of dimer and trimer unbinding. If dimer and trimer unbinding are included, then (M3) only holds for $n \geq 4$, and $\hat{A}_1$ can be obtained from $\hat{A}$ by solving a quartic equation. The resulting model has negligible quantitative difference (at most 20% in the predicted recruitment asymmetry in polarized states) from the one we present here, which is significantly easier to analyze.

[2] This number is similar to that measured for PAR-2 and PAR-6 in [3, Fig. S3]. Considering our measurements (Fig. 2) reveal that roughly half of the bound PAR-3 leaves the membrane after establishment, the maximum percentage of bound protein is 50%, and we take half this number as an estimate. In any case, the results of our model do not change when we change this (arbitrary) assumption.

[3] The parameter h (cytoplasmic "thickness") only appears in the dimensionless parameter $\hat{K}_\mathrm{on}$. Since we fit $\hat{K}_\mathrm{on}$, we never assign a value to h in Table M1.

phases in embryos lacking a functional sperm cue or myosin function, we infer that the spatially uniform steady state is stable. Second, because the polarized state remains stable through maintenance phase in *par-1* mutant embryos, we infer that in the absence of posterior inhibition by PAR-1, PAR-3 dynamics encode the coexistence of spatially uniform and spatially non-uniform (polarized) states. Third, both experiments and simulations show that in the polarized state, the boundary position is stable on timescales relevant to maintenance phase, i.e., the effects of diffusion can be ignored in comparing observed and predicted polarized states. Finally, we observe that the density of membrane bound PAR-3 observed on the anterior cortex during maintenance phase in wild type or *par-1* mutant embryos is roughly the same as that observed throughout the cortex in *spd-5(RNAi)* embryos (Fig. S1) and about eight times that observed on the posterior pole of *par-1* mutant embryos. Thus we seek parameter values satisfying two conditions:

C1: A stable spatially uniform steady state with density $\hat{A}_u$ coexists with a stable spatially non-uniform steady state, characterized by $\hat{A} = \hat{A}_h$ on 50% domain length and $\hat{A} = \hat{A}_\ell$ on the other 50%.

C2: $\hat{A}_h/\hat{A}_\ell \approx 8$ and $\hat{A}_h/\hat{A}_u \approx 1$.

Because model predictions depend upon the form of positive feedback, (encoded by the function $F(\hat{A})$), we next describe the fitting approach and qualitative results for different assumptions about feedback. In all cases, we focus on predicted behavior at/near the spatially uniform and polarized steady states. Neglecting diffusion, and invoking the steady state (M3) for polymerization dynamics reduces the monomer equation (M2a) to the balance of an attachment flux $\delta(\hat{A})$ (which sums the fluxes due to basal attachment and feedback) and a detachment flux $\nu(\hat{A})$,

$$0 = \underbrace{\hat{K}_{\text{on}}\left(1 + \hat{K}_{\text{f}}\hat{F}^{+}(\hat{A})\right)\hat{A}_{\text{c}}}_{\text{Attachment, } \delta(\hat{A})} - \underbrace{\hat{K}_{\text{off}}\hat{A}_1(\hat{A})}_{\text{Detachment, } \nu(\hat{A})} \tag{M7}$$

where $\hat{A}_1(\hat{A})$ is given in (M5). At spatially uniform steady states, $\hat{A}(x) \equiv \hat{A}$, the dimensionless cytoplasmic concentration (defined in (M2d)) becomes $\hat{A}_{\text{c}} = \hat{A}^{(\text{Tot})} - \hat{A}$ (recall $\hat{A}^{(\text{Tot})} = 1$ for wild type embryos), and the total attachment rate is

$$\delta(\hat{A}) = \delta_{\text{cons}}(\hat{A}) = \hat{K}_{\text{on}}\left(1 + \hat{K}_{\text{f}}\hat{F}^{+}(\hat{A})\right)\left(1 - \hat{A}\right) \tag{M8}$$

In this case, the attachment and detachment curves in (M7) depend only on $\hat{A}$, and spatially uniform steady state(s) can be read from their intersections on a flux balance plot (solid red and

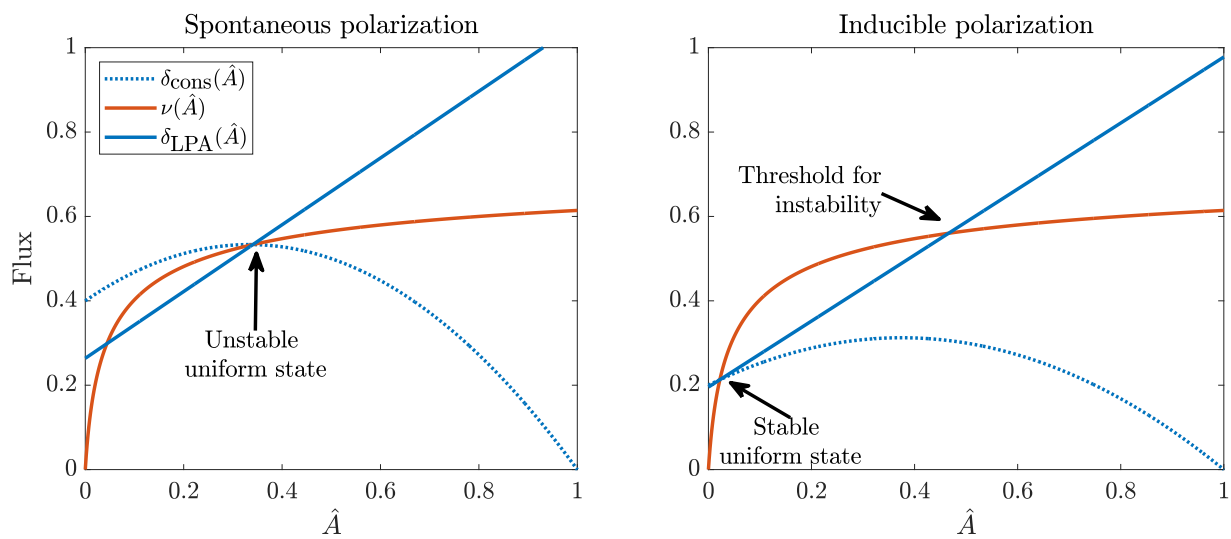

Figure M1: Flux plane analysis for linear feedback model (M10). The uniform state is defined by the single crossing of the attachment rate $\delta_{\rm cons}(\hat{A})$ (dotted blue lines, see (M8)) with the detachment rate $\nu(\hat{A})$ (solid red lines). *Stability* of the uniform state is determined by how the attachment rate $\delta_{\rm LPA}(\hat{A})$ (solid blue lines, see (M9)) compares to $\nu(\hat{A})$ near the steady state. The left panel demonstrates an unstable uniform state, while the right panel demonstrates a stable uniform state with inducible polarization, defined as having the threshold for instability at $\hat{A} \leq 2$.

dotted blue lines in Fig. M1). Following the Local Perturbation Analysis (LPA) approach of [4], we determine stability by considering the response to a local perturbation $\hat{A} = \hat{A}_u + \epsilon\hat{A}$ of finite size within an infinitesimally small domain such that the cytoplasmic concentration remains constant ($\hat{A}_{\rm c} = 1 - \hat{A}_u$). This situation corresponds to an attachment rate of

$$\delta(\hat{A}) = \delta_{\rm LPA}(\hat{A}) = \hat{K}_{\rm on}\left(1 + \hat{K}_{\rm f}\hat{F}^{+}(\hat{A})\right)\left(1 - \hat{A}_u\right). \tag{M9}$$

The qualitative response of the system can be inferred by examining the behavior of $\Delta(\hat{A}) = \delta_{\rm LPA}(\hat{A}) - \nu(\hat{A})$. The case when $\Delta'(\hat{A}_u) > 0$ corresponds to an unstable uniform state, while $\Delta'(\hat{A}_u) < 0$ corresponds to a stable one.

1.3 Linear feedback model

We first consider the linear feedback model that was used previously by some of us [6]

$$f(A) = A \rightarrow \hat{F}(\hat{A}) = \hat{A}. \tag{M10}$$

Using LPA, we determine the qualitative behavior for different values of the two unknown parameters: the basal attachment rate $\hat{K}_{\rm on}$ and the feedback strength $\hat{K}_{\rm f}$. Varying feedback strength

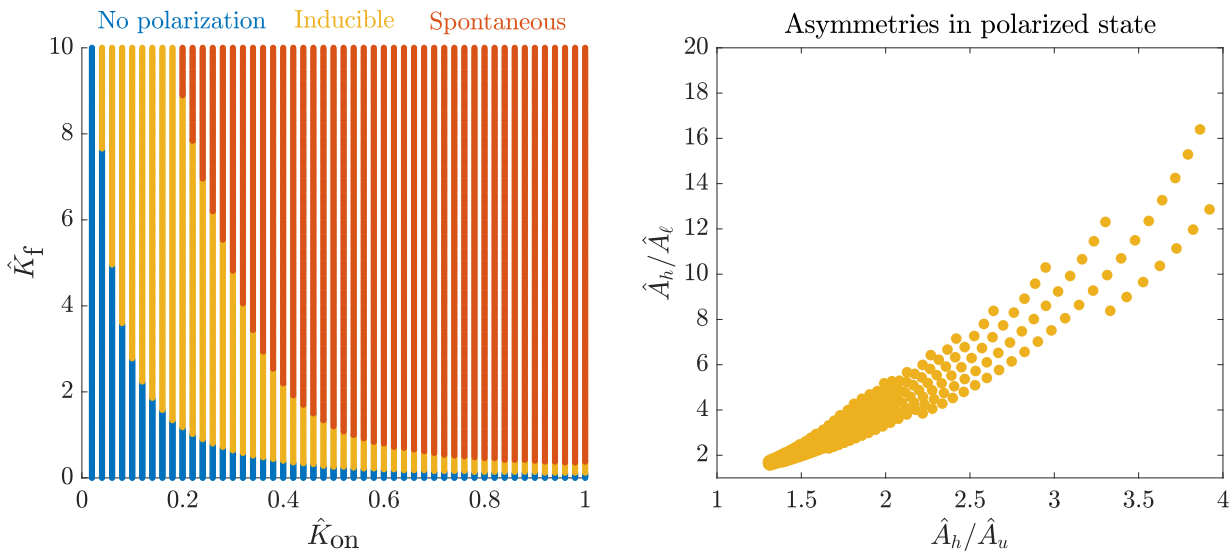

Figure M2: Parameterizing the linear feedback model. At left, we show the phase diagram for the two unknown parameters, $\hat{K}_{\mathrm{on}}$ and $\hat{K}_{\mathrm{f}}$, and break the dynamics into the three regimes of no polarization, inducible polarization, and spontaneous symmetry breaking. Then, at right, we simulate a polarized state with the parameters in the inducible regime. We simulate starting with a 10:1 protein asymmetry with 50% bound protein, then plot the ratios $\hat{A}_h/\hat{A}_u$ and $\hat{A}_h/A_\ell$ after five minutes.

for any fixed basal attachment rate, the qualitative behavior of this system falls into one of three classes (see Figs. M1 and M2):

1. For sufficiently large $\hat{K}_{\mathrm{f}}$, the spatially uniform state is unstable to fluctuations or perturbations of any size (left panel of Fig. M1).

2. For intermediate $\hat{K}_{\mathrm{f}}$, the spatially uniform state is stable to small perturbations, but it is possible to induce polarization by driving the local concentration above a threshold, which is given by a second crossing of attachment and detachment curves in the flux balance plot.

3. Finally, as $\hat{K}_{\mathrm{f}}$ approaches 0, the threshold to induce polarization approaches ∞, and it is essentially impossible to induce polarization.

For the linear model, the phase diagram for polarization (Figure M2) shows that polarity is inducible (a quasi-stable spatially non-uniform steady state exists) for a subset of model parameters. For each reasonable choice of these parameters (specifically, choices which yield a uniform state with mean oligomer size between 2.5 and 3.5), we determine the polarized "steady state" from asymmetric initial conditions (10:1 initial asymmetry on 50% of the domain with 50% of the total protein initially bound) by simulating for five minutes and evaluating the ratios $\hat{A}_h/\hat{A}_\ell$ and $\hat{A}_h/\hat{A}_u$.

We find that none of the parameter values yielding inducible polarity give ratios of $\hat{A}_h/\hat{A}_\ell$ and $\hat{A}_h/\hat{A}_u$ that match those observed empirically. In essence, for the linear model to achieve five-to-ten-fold ratio of densities in the non-uniform steady state, the higher density must be significantly (2 to 3.5 times) higher than that observed in the spatially uniform steady state, since it must be large enough to overcome the threshold required to induce polarization (this is the scenario depicted in the right panel of Fig. M1).

1.4 Saturated feedback model

Our experimental finding that PAR-3 recruitment asymmetries do not change during maintenance phase as levels of membrane-bound PAR-3 fall by $\approx 50\%$ suggest that positive feedback saturates at or below the density observed in late maintenance. Thus, we consider a simple model for saturating feedback given by

$$f(A) = \min\left(A, A^{(\mathrm{Sat})}\right) \to \hat{F}(\hat{A}) = \min\left(\hat{A}, \hat{A}^{(\mathrm{Sat})}\right), \tag{M11}$$

where $\hat{A}^{(\mathrm{Sat})} < \hat{A}_u$.

As in the case for linear feedback, we use the saturated feedback function (M11) to identify spatially uniform steady states as solutions of the flux balance equation (M7) with $\delta = \delta_{\mathrm{cons}}(\hat{A})$ given in (M8). We then evaluate the stability of the uniform state using LPA; as shown in the flux balance plot in Fig. M3, if the feedback saturates below the spatially uniform steady state concentration, the spatially uniform steady state is always stable. However, for a subset of values of ($\hat{K}_{\mathrm{on}}$, $\hat{K}_{\mathrm{f}}$ and $\hat{A}^{(\mathrm{Sat})}$), polarity can be induced by local perturbations that drive $\hat{A}$ *below* some threshold. In this case, at the stably polarized steady state, $\hat{A}_\ell$ lies below the threshold for inducing polarity, while $\hat{A}_h$ is held close to spatially uniform density $\hat{A}_u$ by saturating feedback, making it possible to satisfy conditions C1 and C2 ($\hat{A}_h/\hat{A}_\ell \approx 8$ and $\hat{A}_h/\hat{A}_u \approx 1$) from above.

To select values for $\hat{K}_{\mathrm{on}}$, $\hat{K}_{\mathrm{f}}$ and $\hat{A}^{(\mathrm{Sat})}$, we first observe that $\hat{A}^{(\mathrm{Sat})}$ cannot lie too far below $\hat{A}_h$, since otherwise the threshold crossing that defines inducible polarity in the LPA flux balance curves (Fig. M3) cannot occur. We therefore begin by setting the saturation threshold at $\hat{A}^{(\mathrm{Sat})} = 0.8\hat{A}_u$. Then, we scan over all pairs of $\left(\hat{K}_{\mathrm{on}}, \hat{K}_{\mathrm{f}}\right)$ to find a polarized state with anterior concentration $\hat{A}_h \approx 0.4$ (which, because of our fitting of the depolymerization curve, gives $\alpha = 0.73$ on the anterior) and an A/P ratio of approximately 8. As in the linear feedback model, the scan happens in two steps (Fig. M4): we first make a phase diagram separating into regimes with no polarization and bistable dynamics. Then, we study the polarized states by repeating the same set of simulations we used for the linear model, where we evolve an initial 10:1 asymmetry in time and plot the ratios

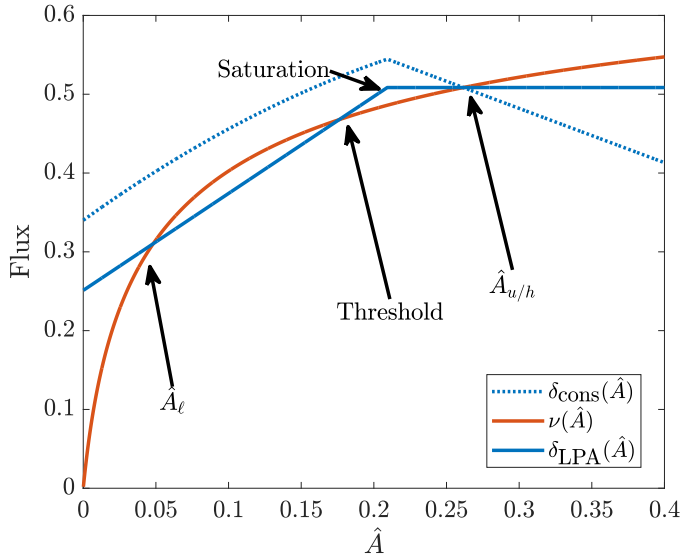

Figure M3: Flux plane analysis for linear feedback model with saturation at 80% of uniform state. As in Fig. M1, the uniform state is determined by the crossing of $\delta_{\text{cons}}(\hat{A})$ and $\nu(\hat{A})$, while the stability of the uniform state is determined by $\delta_{\text{LPA}}(\hat{A})$. The uniform state is stable if the feedback saturates below it.

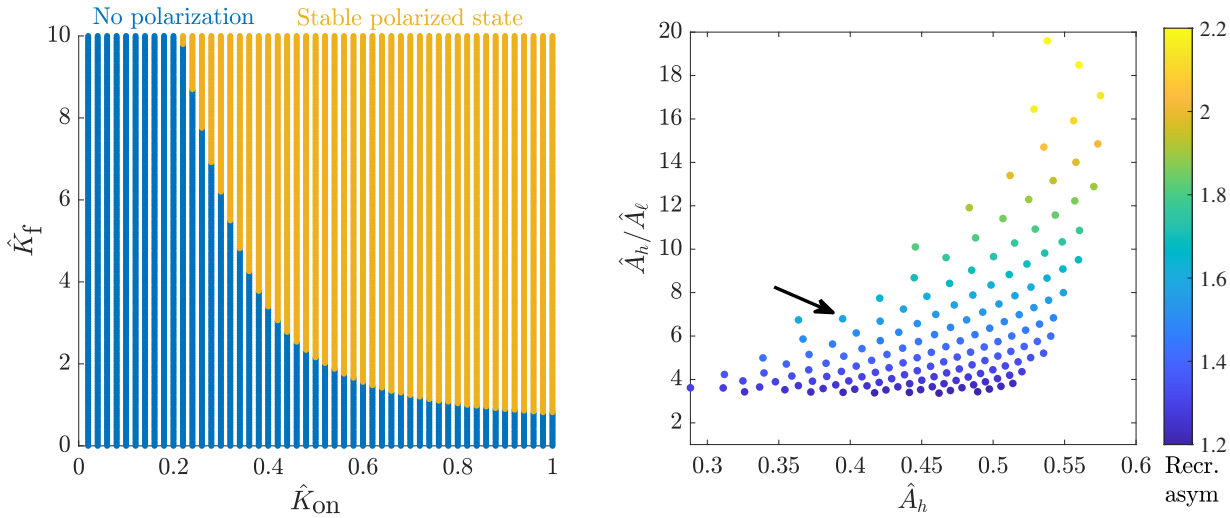

Figure M4: Parameterizing the linear feedback model with saturation, given $\hat{A}^{(\text{Sat})} = 0.8\hat{A}_u$. (Left:) Phase diagram for the two unknown parameters, $\hat{K}_{\text{on}}$ and $\hat{K}_{\text{f}}$. We break the dynamics into the two regimes of no polarization (one crossing of $\delta_{\text{LPA}}(\hat{A})$ and $\nu(\hat{A})$ in the flux balance plot), and bistable dynamics (three crossings). (Right:) We simulate the polarized state by starting from a 10:1 initial asymmetry on 50% of the domain with 50% of the total protein bound, then running forward in time. We plot the ratios $\hat{A}_h/\hat{A}_u$ and $\hat{A}_h/A_\ell$, colored by the recruitment asymmetry, $\delta(\hat{A}_h)/\delta(A_\ell)$, all after five minutes. Black arrow shows our chosen parameters.

Parameter	Description	Value	Units	Ref	Notes
L	Domain length	134.6	μm	[2]	radii 27×15 μm ellipse
D_1	Monomeric PAR-3 diffusivity	0.1	$\mu\text{m}^2/\text{s}$		This study
$\hat{K}_{\text{on}}$	Monomeric PAR-3 attachment rate	0.34			Fitting
$\hat{K}_{\text{f}}$	Feedback strength	4.9			Fitting
$\hat{A}^{(\text{Sat})}$	Feedback saturation level	0.21			80% of uniform state in wild type
k_{off}	Monomeric PAR-3 detachment rate	3	1/s		This study, Fig. 3K
k_{dep}	PAR-3 depolymerization rate	0.16	1/s		This study, Fig. 4E
$\hat{K}_{\text{p}}$	PAR-3 polymerization rate	25			Fit $\alpha = 0.73$ with $\hat{A} = 0.4$
N	Max oligomer size	50			Same results for larger N

Table M1: Parameter values for the PAR-3 model (see (M2e) for the definitions of dimensionless parameters).

$\hat{A}_h/\hat{A}_u$ and $\hat{A}_h/A_\ell$ after five minutes (again only simulating with parameters that have a mean oligomer size between 2.5 and 3.5 in the uniform state). Fig. M4 shows that a choice of parameters ($\hat{K}_{\text{on}} = 0.34$, $\hat{K}_{\text{f}} = 4.9$) exists which satisfies $\hat{A}_h = 0.4$ with an A/P ratio of 7. This choice gives a recruitment asymmetry of 1.6 after 5 minutes, which is about 80% of the value we measured experimentally, and a wild-type uniform state of $\hat{A}_u = 0.26$, with corresponding feedback saturation level $\hat{A}^{(\text{Sat})} = 0.8\hat{A}_u \approx 0.21$. Table M1 summarizes the parameters.

We note that the (arbitrary) choice of saturation level and anterior concentration $\hat{A}_h$ make little difference in our model, as changes in these parameters simply give different choices of $\hat{K}_{\text{on}}$ and $\hat{K}_{\text{f}}$ that satisfy the desired conditions. More fundamentally, the saturating feedback model gives a ratio $\hat{A}_h/\hat{A}_u \approx 1.5$, so that the anterior state concentration exceeds that of the uniform state by only 50%, relative to 100–200% in the linear feedback model. Unlike in the linear model, where such a change was necessary to surpass the threshold for polarization, here the change is just a consequence of a higher cytoplasmic concentration (and thus a higher attachment rate, which comes into equilibrium with the nonlinear detachment curve).

1.5 Phase diagram

In order to compare the model to experimental data, we use simulations of the polarized state to construct a phase diagram of the stability behavior as a function of the mean oligomer size and feedback strength in Fig. 7B. To generate the phase diagram, we vary $\hat{K}_{\text{p}}$, $\hat{K}_{\text{on}}$, and $\hat{K}_{\text{f}}$, compute the uniform state, and assign the feedback saturation level. Simulated states are defined to be

"polarized" if the A/P ratio is larger than 2 after $t = 5$ mins of simulation time. Data points are plotted based on the "feedback strength"

$$\text{Feedback strength} = \hat{K}_{\mathrm{f}}\hat{F}^{+}(\hat{A}) = \frac{k_f}{k_{\mathrm{basal}}} \min\left(\hat{A}, \hat{A}^{(\mathrm{Sat})}\right) = \frac{k_f \hat{A}^{(\mathrm{Sat})}}{k_{\mathrm{basal}}},$$

(the last equality holds since in the polarized state $\hat{A}_h > \hat{A}_u > \hat{A}^{(\mathrm{Sat})}$), and mean oligomer size

$$\text{Mean oligomer size} = \left(\sum_{n=1}^{N} n\hat{A}_n\right) / \left(\sum_{n=1}^{N} \hat{A}_n\right),$$

at $t = 5$ mins. The phase diagram shows that bistability is possible at smaller feedback strengths if the mean oligomer size is large enough, and vice versa.

2 Dynamics

We use standard numerical methods to solve (M2), discretizing the one-dimensional domain at N points, with diffusion being discretized via the standard three point Laplacian. We use a forward Euler method for the reaction terms, and a backward Euler method for the diffusion terms (in the monomer equation), which gives first order accuracy in time [5, c. 1]. Typical parameters are $N = 1000$ (required to resolve the boundary layer where the enriched PAR-3 domain can shift) and $\Delta\hat{t} = 0.02$ (50 steps per depolymerization time). Matlab code is available at the github repository `https://github.com/omaxian/CElegansModel/`.

We first simulate our PAR-3 model with two different initial conditions (Fig. M5): a perturbation of the uniform state (which demonstrates that the uniform state is a stable attractor) and a polarized state with all protein initially bound, which decays to a stable polarized state. In both cases, the timescale on which the protein levels adjust is roughly 5–10 minutes.

2.1 Slow drift of the boundary

In our simulation of the polarized state in Fig. M5, we notice the appearance of a drift of the boundary in time. This drift, which is controlled by diffusion, appears to be much slower than the equilibration of concentration. To understand it in more detail, in Fig. M6 we plot the evolution of a polarized PAR-3 domain of various initial sizes (beginning with a 10:1 asymmetry and 50% protein bound), recording the ratio $\hat{A}_h/\hat{A}_\ell$, as well as the overall domain size. There we see rapid (timescale roughly 5–10 minutes) equilibration of the initial concentrations, followed by a slow drift (timescale much longer than 60 minutes) of the boundary to a unique position. Note that even

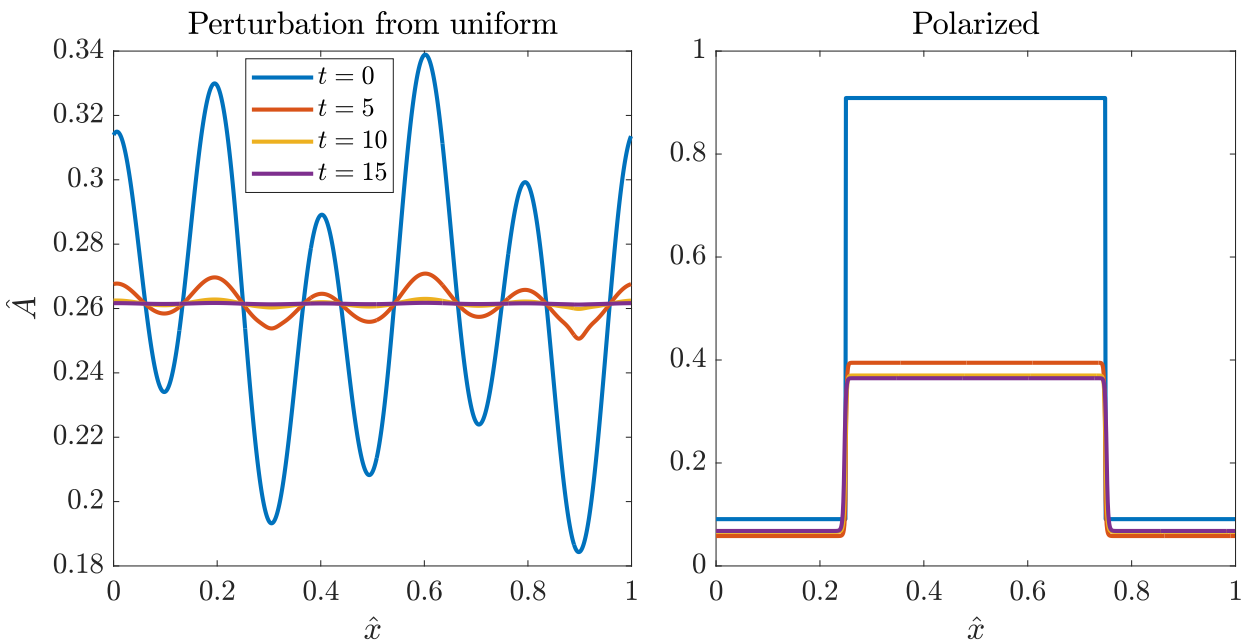

Figure M5: Dynamics of the saturated feedback model. At left, we show that perturbations to the uniform state decay, while at right, we show that the polarized state is stable in time. Dynamics occur on timescales of 5–10 minutes (legend).

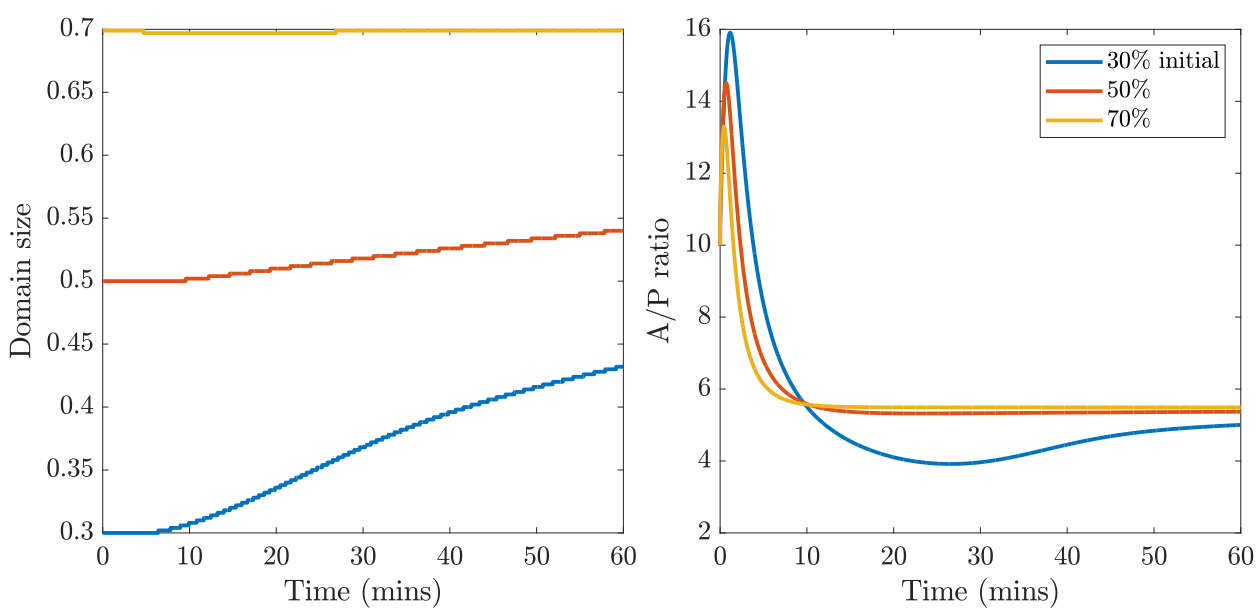

Figure M6: Dynamics of an initially polarized domain. We consider initial enriched domain sizes of 30, 50, and 70%, and impose a 10:1 asymmetry at $t = 0$ with 50% protein bound to the membrane to mimic the end of establishment phase. We then track the enriched domain size and $\hat{A}_h/\hat{A}_\ell$ over time. There is a relatively fast timescale of concentration equilibration, followed by slow boundary drift.

the "fast" shift in concentrations, which occurs on a scale of 5–10 minutes, is still slow enough to compete with the timescale of maintenance phase. That is, even at the end of maintenance phase, the concentrations are still likely transitioning to the steady state.

2.2 Systematic depletion of PAR-3

To model the experiment of PAR-3 depletion (Fig. 7), we vary the total fraction of PAR-3 $\hat{A}^{(\mathrm{Tot})}$. To simulate experimental conditions for a given $\hat{A}^{(\mathrm{Tot})}$, we start at the "end of establishment phase," which corresponds to 50% protein bound to the membrane and a roughly 10:1 ratio of anterior to posterior protein and an anterior domain size of 50% (this the dark blue protein profile in the right panel of Figs. M5). We then run forward in time until we reach $t = 4$ minutes, corresponding exactly to the time interval used in experiments, after which we record the mean oligomer size on the enriched domain, and the A/P ratio. Because the dimensionless parameters in (M2e) are in terms of the total PAR-3 in *wild-type* embryos, only $\hat{A}^{(\mathrm{Tot})}$ changes when we perform the depletion experiment.

The results in Fig. 7 show that our model successfully reproduces the trend in mean oligomer size vs. total bound density (on the anterior). For the A/P asymmetries, our model captures the qualitative and quantitative trend of no asymmetry for low mean oligomer sizes, followed by a transition to stable asymmetries on the order 6–8 for larger mean oligomer sizes. This is in contrast to a model based on asymmetric recruitment (in which case there is no feedback and monomers are recruited to the anterior at 1.7 times the rate of the posterior), which predicts a persistent asymmetry even as the mean oligomer size drops to 1 (i.e., even without oligomerization).

2.3 Changing feedback to mimic aPAR depletion

Finally, we use our saturated feedback model to demonstrate what might happen when the feedback is reduced, in order to explain the results of some of our perturbation experiments. To do this, we perturb the feedback parameter $\hat{K}_{\mathrm{f}}$ and examine changes to the flux balance plot (Fig. M7) and dynamics of an initially polarized state (10:1 asymmetry with 50% protein bound; main text Fig. 8). We are already familiar with the flux balance plot for wild type parameters (Fig. M3). Simulating maintenance phase with these parameters yields the expected dynamics: the anterior domain concentration decreases, while the posterior remains roughly constant, and there is a steady state asymmetry (solid lines in the bottom panel).

Reducing to 0% feedback ($\hat{K}_{\mathrm{f}} = 0$) gives dynamics which correspond roughly to our experiment

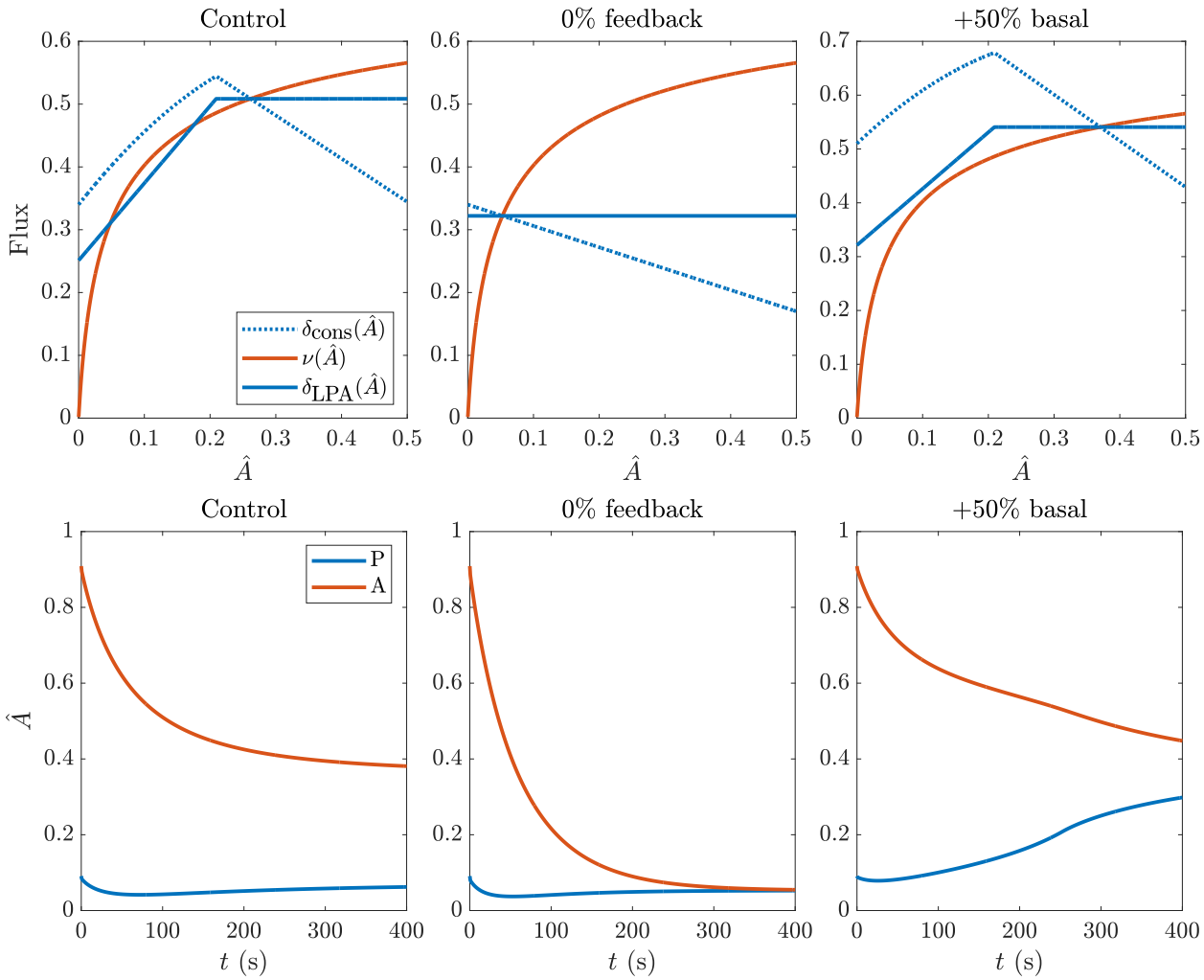

Figure M7: How the system responds to reductions in feedback and changes in the basal rate. Top plots: theoretical flux balance when considering default parameters ($\hat{K}_{\text{f}} = 4.9$, $\hat{K}_{\text{on}} = 0.34$), 0% feedback ($\hat{K}_{\text{f}} = 0$, $\hat{K}_{\text{on}} = 0.34$), and 150% basal binding rate ($\hat{K}_{\text{f}} = 3.3$, $\hat{K}_{\text{on}} = 0.51$). Bottom plot: trajectory of an initially 10:1 polarized state (split over half the embryo length with 50% bound protein) over time.

with PAR-6 depletion (RNAi). In this case, removing feedback gives a single, smaller, uniform steady state which is close to posterior levels in the wild type. In simulations (Fig. 8), we consequently observe a convergence of the anterior and posterior levels onto a smaller concentration, near to the original posterior level.

For CDC-42 depletion (RNAi), we hypothesize that an increase in the basal binding rate could lead to a loss of asymmetry. To test this, we increase k_{basal} by 50%; using the non-dimensionalization in (M2), this implies $\hat{K}_{\text{on}}$ increases by 50% and $\hat{K}_{\text{f}}$ decreases by 33%. As shown in the top right panel in Fig. M7, the effect of this change is to increase the y intercept of the local flux balance curve δ_{LPA}, which leads to a loss of bistability. As shown in the bottom right panel of Fig. M7, the dynamics with this choice of parameters roughly correspond to our experiment in CDC-42 (RNAi) embryos, where the posterior state rises up to meet the anterior one.

References

[1] Leah Edelstein-Keshet and G Bard Ermentrout. Models for the length distributions of actin filaments: I. simple polymerization and fragmentation. *Bulletin of mathematical biology*, 60(3):449–475, 1998.

[2] Nathan W Goehring, Philipp Khuc Trong, Justin S Bois, Debanjan Chowdhury, Ernesto M Nicola, Anthony A Hyman, and Stephan W Grill. Polarization of par proteins by advective triggering of a pattern-forming system. *Science*, 334(6059):1137–1141, 2011.

[3] Peter Gross, K Vijay Kumar, Nathan W Goehring, Justin S Bois, Carsten Hoege, Frank Jülicher, and Stephan W Grill. Guiding self-organized pattern formation in cell polarity establishment. *Nature physics*, 15(3):293–300, 2019.

[4] William R Holmes, May Anne Mata, and Leah Edelstein-Keshet. Local perturbation analysis: a computational tool for biophysical reaction-diffusion models. *Biophysical journal*, 108(2):230–236, 2015.

[5] Willem H Hundsdorfer, Jan G Verwer, and WH Hundsdorfer. *Numerical solution of time-dependent advection-diffusion-reaction equations*, volume 33. Springer, 2003.

[6] Charles F Lang and Edwin M Munro. Oligomerization of peripheral membrane proteins provides tunable control of cell surface polarity. *Biophysical Journal*, 121(23):4543–4559, 2022.